



**HAL**  
open science

## **Archean to Paleoproterozoic crustal evolution in the Sassandra-Cavally domain (Côte d'Ivoire, West Africa): Insights from Hf and U-Pb zircon analyses**

Augustin Y. Koffi, Nicolas Thébaud, Alain Kouamelan, Lenka Baratoux,  
Olivier Bruguier, Olivier Vanderhaeghe, Pavel Pitra, Anthony I.S. Kemp,  
Noreen Evans

### ► To cite this version:

Augustin Y. Koffi, Nicolas Thébaud, Alain Kouamelan, Lenka Baratoux, Olivier Bruguier, et al.. Archean to Paleoproterozoic crustal evolution in the Sassandra-Cavally domain (Côte d'Ivoire, West Africa): Insights from Hf and U-Pb zircon analyses. *Precambrian Research*, 2022, 382, pp.106875. 10.1016/j.precamres.2022.106875 . insu-03820412

**HAL Id: insu-03820412**

**<https://insu.hal.science/insu-03820412v1>**

Submitted on 20 Oct 2022

**HAL** is a multi-disciplinary open access archive for the deposit and dissemination of scientific research documents, whether they are published or not. The documents may come from teaching and research institutions in France or abroad, or from public or private research centers.

L'archive ouverte pluridisciplinaire **HAL**, est destinée au dépôt et à la diffusion de documents scientifiques de niveau recherche, publiés ou non, émanant des établissements d'enseignement et de recherche français ou étrangers, des laboratoires publics ou privés.

# Archean to Paleoproterozoic crustal evolution in the Sassandra-Cavally domain (Côte d'Ivoire, West Africa): insights from Hf and U-Pb zircon analyses

Augustin Y. Koffi<sup>1</sup>, Nicolas Thébaud<sup>2</sup>, Alain N. Kouamelan<sup>1</sup>, Lenka Baratoux<sup>3,1</sup>, Olivier Bruguier<sup>4</sup>, Olivier Vanderhaeghe<sup>3</sup>, Pavel Pitra<sup>5,6</sup>, Anthony I.S. Kemp<sup>2</sup>, Noreen Evans<sup>7</sup>

<sup>1</sup>UFHB Abidjan-Cocody. UFR STRM. 22 BP 582 Abidjan 22. Côte d'Ivoire, [yaoaugustinkoffi@yahoo.fr](mailto:yaoaugustinkoffi@yahoo.fr);

<sup>2</sup>University Western Australia. School of Earth Sciences, Centre for Exploration Targeting, Australia. 35 Stirling highway, WA6009 Crawley

<sup>3</sup>GET, Université de Toulouse, CNRS, IRD, UPS, (Toulouse), France

<sup>4</sup>Géosciences Montpellier. Université Montpellier - CNRS. cc 060. Place Eugène Bataillon. 34095 Montpellier Cedex 5. France.

<sup>5</sup>Univ Rennes, CNRS, Géosciences Rennes - UMR 6118, F-35000 Rennes, France.

<sup>6</sup>Czech Geological Survey, Klárov 3, CZ-118 21 Praha 1, Czech Republic.

<sup>7</sup>John DeLaeter centre Curtin University

## Abstract

Crustal evolution in the south West African Craton is dominated by a significant input of juvenile material into the crust at ca. 2.1 Ga and it remains unclear how much of the Paleoproterozoic continental mass was influenced by the presence of pre-existing Archean crustal domains. The Sassandra-Cavally (SASCA, Côte d'Ivoire) domain is strategically located east of the Sassandra shear zone at the transition of the Paleoproterozoic and Archean terranes of the Leo-Man shield. Combined U-Pb and Lu-Hf isotopic analyses by LA-(MC-)ICP-MS were acquired on zircon grains extracted from migmatitic gneisses, metasedimentary rocks and a granitic intrusion.

The migmatitic gneisses, yield Archean ages between ca. 3330 and 2810 Ma with  $\epsilon_{\text{Hf}}$  ranging from -9.4 to +3.3 and a metamorphic age at  $2076 \pm 6$  Ma. They are tentatively interpreted as orthogneisses extracted from the mantle during the Paleoproterozoic and reworked substantially in the Mesoarchean. Detrital zircon grains from metasedimentary units adjacent to the Archean migmatitic gneisses yield ages ranging from ca. 2213 to 2088 Ma with  $\epsilon_{\text{Hf}}$  ranging from +0.0 to +5.5, indicating derivation from juvenile Paleoproterozoic source rocks. A granite intrusion was dated within uncertainty of the metamorphic age at  $2084 \pm 6$  Ma. It exhibits a hybrid isotopic signature with  $\epsilon_{\text{Hf}}$  forming two distinct clusters between -4.9 and -8.5, and between +2.2 and +6.5 for inherited zircon grains dated between ca. 2343 to 2100 Ma.

The near continuous U-Pb age record from this early Mesoarchean event to the Neoproterozoic is associated with constant initial  $^{176}\text{Hf}/^{177}\text{Hf}$  suggesting for an ancient lead loss event at ca. 2800 Ma or a prolonged period of zircon dissolution/precipitation and/or crystallization. This early

period is followed by peaks of zircon dates highlighting crustal extraction during the Eoeburnean (ca. 2250 to 2150 Ma) and Eburnean orogenies (ca. 2140 to 2100 Ma). The absence of detrital zircon of the ages similar to those of migmatitic gneisses (~3200–2800 Ma) in Paleoproterozoic metasediments suggests their deposition distal from the Archean terranes followed by a tectonic assemblage of the SASCA domain during the later stages of the Eburnean orogeny.

**Key words:** zircon geochronology; U-Pb and Lu-Hf isotopes; juvenile crustal growth, crustal growth and reworking; Archean; West African Craton; Côte d'Ivoire.

## 1. INTRODUCTION

According to some authors, from 50 to 80 % of the Earth's continental crust formed prior to ~2.5 Ga (Armstrong et al., 1991; Belousova et al., 2010; Dhuime et al., 2012; Hawkesworth et al., 2010; Korenaga, 2018). The period between 2.1 Ga and 1.8 Ga following the early growth of the continental crust is associated with the assembly of the Earth's first coherent supercontinent Columbia (Ledru et al., 1994; Meert, 2012; Nance et al., 2014; Santosh, 2010; Zhao et al., 2002). Over that time period significant juvenile crustal extraction has globally been documented throughout the world including the Guyana Shield (da Rosa-Costa et al., 2006; Delor et al., 2003; Gruau et al., 1985; Klein and Rodrigues, 2021; Milhomem Neto and Lafon, 2019, 2020; Vanderhaeghe et al., 1998) and the West African Craton (Abouchami et al., 1990; Block et al., 2016; Eglinger et al., 2017; Grenholm et al., 2019; Parra-Avila et al., 2016, 2017; Petersson et al., 2016, 2018). In the West African Craton, the Archean and Paleoproterozoic shields crop out beneath the vast Neoproterozoic-Paleozoic Taoudeni basin as the Reguibat Shield in the north, the Leo-Man Shield in the south (Berger et al., 2013; Jessell et al., 2015; Potrel et al., 1996; Rocci, 1965; Thiéblemont, 2016) and the Paleoproterozoic Kayes and Kedougou-Kénieba Inliers between the two shields (Gärtner et al., 2017; **Fig. 1**). Archean terrains of the West African Craton are dominated by gneisses and display an exceptionally thick subcontinental lithosphere estimated between 180 and 240 km (Jessell et al., 2016; McKenzie and Priestley, 2008), and associated with the presence of eclogites in kimberlites, and high-potassic plutonic rocks (Laurent et al., 2016). The gneissic domains exhibit a prolonged geological history and underwent significant reworking events during the Archean at ca. 3500 Ma, 3260–3050 Ma and 2960–2850 Ma (Barth et al., 2002; Beckinsale et al., 1980; Bering et al., 1998; Cahen et al., 1984; Camil, 1984; Camil et al., 1983; Eglinger et al., 2017; Kouamelan et al., 1997a, 1997b, 2015; MacFarlane et al., 1981; Potrel et al., 1998; Rollinson,

2018, 2016; Rollinson and Cliff, 1982; Thiéblemont et al., 2004; Vachette et al., 1973) and during the Paleoproterozoic at ca. 2200–2100 Ma (Block et al., 2016; Gouedji et al., 2014; Grenholm et al., 2019; Kouamelan et al., 2018; Liégeois et al., 1991; Parra-Avila et al., 2016; Petersson et al., 2018, 2016; Pitra et al., 2010; Wane et al., 2018). Yet, the nature and timing of the crustal evolution process and accuracy of geochronological data in terms of growth events and/or crustal reworking that punctuated the West African Craton (WAC) from the Mesoarchean to the Paleoproterozoic still remain poorly constrained.

A locality that may help to shed some light on the WAC crustal evolution process is the region situated in the Archean-Paleoproterozoic transition zone situated at the border between the Kenema-Man and the Baoulé-Mossi domains, separated by the Sassandra shear zone (Abouchami et al., 1990; Bessoles, 1977; Camil, 1984; Feybesse and Milési, 1994; Kouamelan et al., 1997a; Kouamelan, 1996; Peucat et al., 2005; Thiéblemont et al., 2004, 2001) (**Fig. 2**). This transition zone extends from the Baoulé-Mossi domain in western Côte d'Ivoire and southern Guinea, respectively east or north of the Sassandra shear zone (Eglinger et al., 2017; Koffi, 2019; Kouamelan et al., 2018). The gneisses with Archean U-Pb zircon ages found in this zone are interpreted to represent Archean crustal blocks remobilized during the Paleoproterozoic Eburnean orogeny, yet the timing of events and magmatic reservoirs involved remains poorly constrained (Gouedji et al., 2014; Kouamelan et al., 1997a, 1997b, 2015; Pitra et al., 2010; Triboulet and Feybesse, 1998). One of these Archean crustal blocks, referred to as the SASCA domain (Kouamelan, 1996), is located to the southwest of Côte d'Ivoire, and is the focus of this study.

Over the past decade, analysis of U-Pb and Lu-Hf isotopes in zircon have proven to be powerful tools for constraining the growth and reworking of the continental crust (Amelin et al., 1999, 2000; Belousova et al., 2010; Condie, 2013; Condie et al., 2011; Condie and Aster, 2013; Harrison et al., 2005, 2008; Hawkesworth et al., 2010; Kemp et al., 2010; Maas et al., 1992; Nebel-Jacobsen et al., 2010; Parra-Avila et al., 2016; Petersson et al., 2016; Zeh et al., 2014). Zircon can survive several metamorphic, igneous and sedimentary cycles and through its isotopic record, it documents crust formation and its subsequent evolution (Bouilhol et al., 2011, 2013; Condie et al., 2011; Roberts and Spencer, 2015). The analyses of U-Pb and Lu-Hf isotope compositions within the same zircon growth domain give access to both the age and the Hf isotopic signature of the zircon at the time of its crystallization (Griffin et al., 2002; Woodhead et al., 2004) and provide a better understanding of the timing of magma generation with respect to the age of the source (e.g. Hawkesworth and Kemp, 2006).

In order to evaluate the crustal evolutionary process in the WAC, we present combined U-Pb and Lu-Hf isotopic analyses acquired by laser ablation inductively coupled plasma mass spectrometry (LA-(MC)-ICP-MS) on zircon grains from the Sassandra-Cavally (SASCA) domain located to the east of the Sassandra shear zone. Our results illustrate the complex crustal evolution processes combining juvenile mantle extraction and crustal reworking that led to the emergence and stabilization of the West African Craton from the Paleoproterozoic through to the Paleoproterozoic.

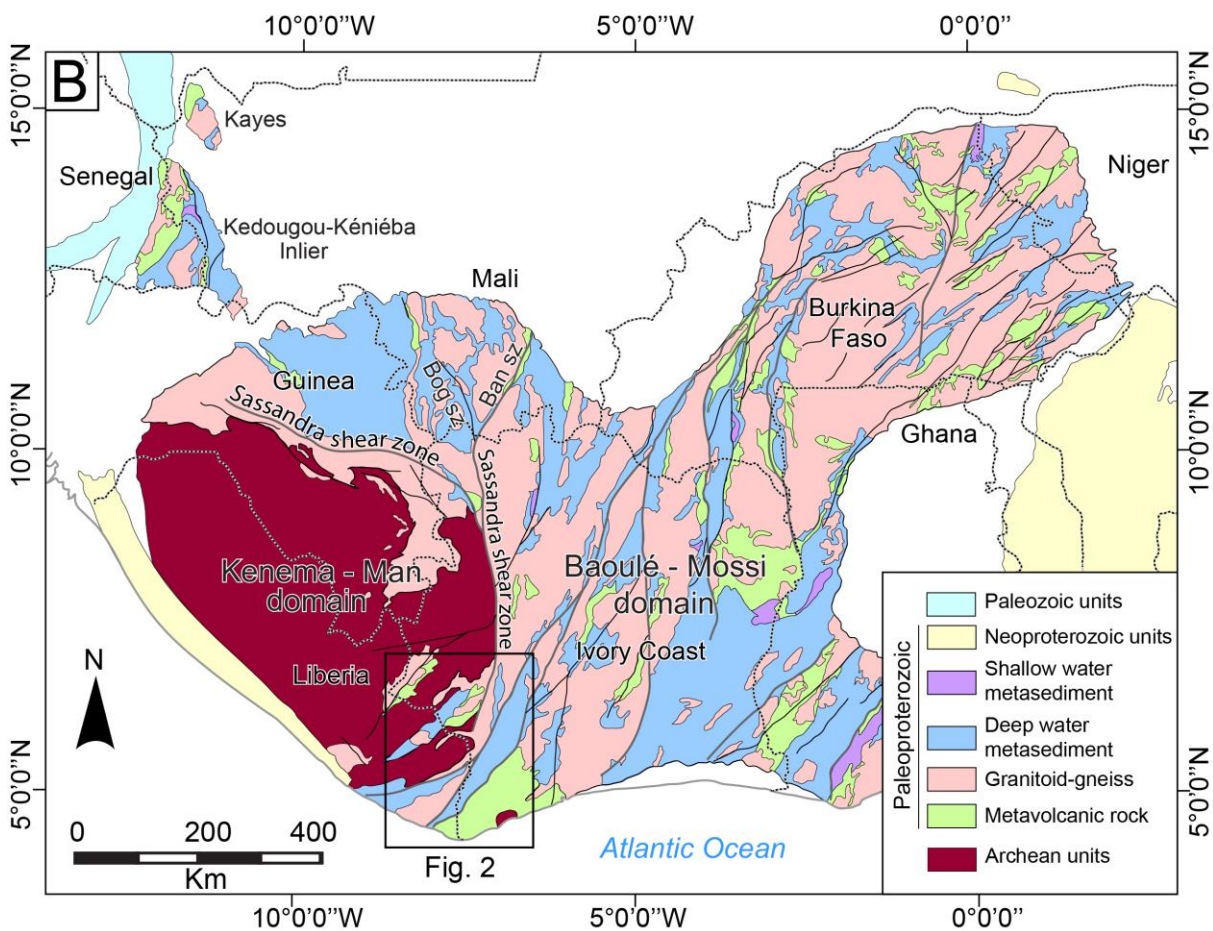
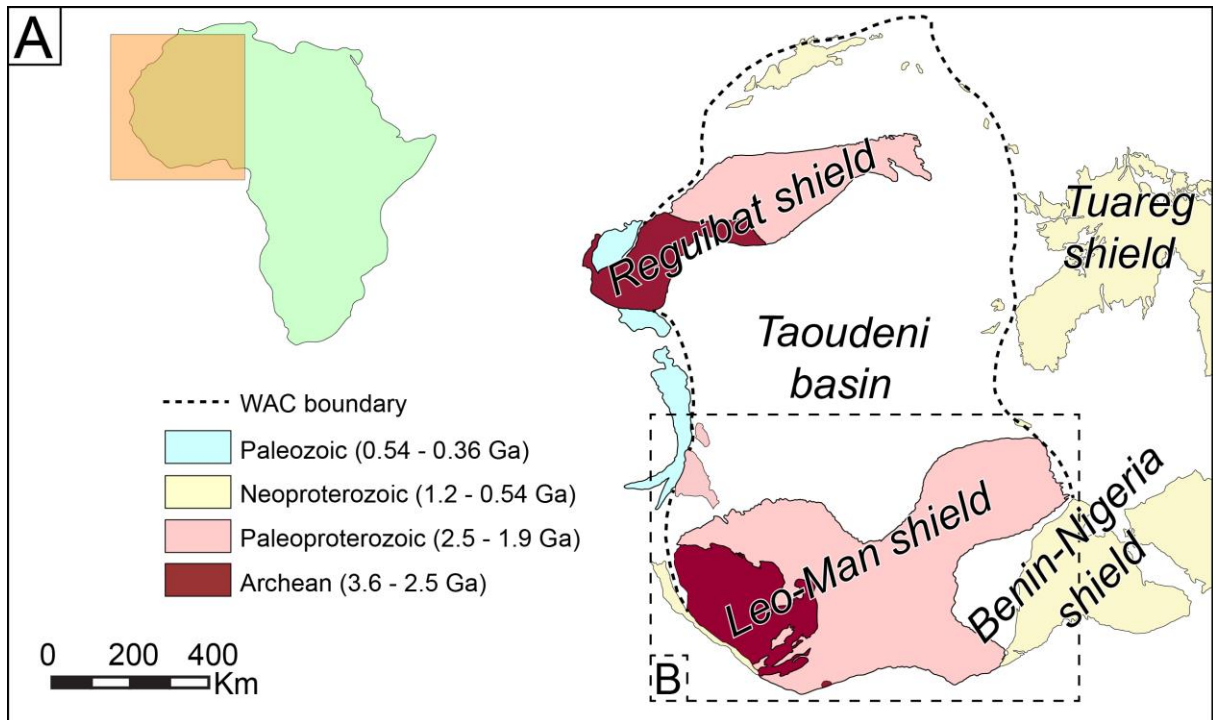


**Fig. 1.** (A) Simplified geological map of the West African Craton (modified after Grenholm, 2014). The position of the present-day margins of the craton are constrained by geophysical data (Jessell et al., 2016), (B) Simplified geological map of the Leo-Man Shield (modified after

Agyei et al., 2009; Baratoux et al., 2011; Egal et al., 2002; Grenholm, 2014; Thiéblemont, 2016). Bog sz: Bougouni shear zone; Ban: Banifing shear zone.

## 2. GEOLOGICAL SETTING

The Leo-Man Shield consists of the Kenema-Man domain in the west, made of Archean terranes, and the Baoulé-Mossi domain in the east, made of Paleoproterozoic formations designated as the Birimian (Auvray et al., 1992; Bessoles, 1977; Milési et al., 1989; Thiéblemont et al., 2004). The Kenema-Man domain covers Liberia, Sierra Leone and part of Guinea as well as Côte d'Ivoire and is dominated by plutons of tonalite-trondhjemite-granodiorite (TTG), gneissic domains and meta volcano-sedimentary belts composed of metasedimentary and metavolcanic rocks that underwent amphibolite to granulite facies matamorphism (Barth et al., 2002; Camil, 1981, 1984; Gouedji et al., 2014; Pitra et al., 2010). The metavolcanic-sedimentary belts are bound by shear zones and alternate with TTG-type granitoids, granites and gneissic domains. The Kenema-Man domain gneisses display U-Pb zircon ages ranging from ca. 3600 to 2600 Ma (Gouedji et al., 2014; Milési et al., 1992; Rollinson, 2016, 2018; Thiéblemont et al., 2001, 2004) that were initially interpreted to be the result of two orogenic cycles, the Leonian (~ 3400–3000 Ma) and the Liberian (~ 2900–2700 Ma) (Barth et al., 2002; Egal et al., 2002; Koffi et al., 2020; Milési et al., 1989; Thiéblemont et al., 2004). Recent work conducted in the Kenema-Man Domain by Rollinson (2016) has further documented zircon age clusters at ca. 3500 Ma, ca. 3260–3050 Ma and ca. 2960–2850 Ma, interpreted as several distinct magmatic events. The older ages are also found in xenocrystic zircon cores in younger rocks suggesting a partial reworking of the older domains.

The Baoulé-Mossi domain records the formation of a large volume of continental crust between ca. 2300 and 2070 Ma and covers Burkina Faso, Ghana and parts of Côte d'Ivoire, Mali, Guinea, Niger and Togo (Abouchami et al., 1990; Boher et al., 1992; Egal et al., 2002). This area consists of deformed and metamorphosed volcanic (tholeiitic and calc-alkaline), volcano-sedimentary and sedimentary rock, all intruded by different generations of granitic rocks showing overall Paleoproterozoic juvenile Nd as well as Hf isotopic signatures (Abouchami et al., 1990; Ama Salah et al., 1996; Baratoux et al., 2011; Béziat et al., 2000; Doumbia et al., 1998; Feybesse et al., 2006; Ganne et al., 2014; Gasquet et al., 2003; Hirdes et al., 1996; Liégeois et al., 1991; Parra-Avila et al., 2016; Pouclet et al., 2006; Tapsoba et al., 2013; Vidal et al., 2009). Deformation and metamorphism of these rocks has been attributed to the Eoeburnean (~2250 to 2150 Ma) and Eburnean orogenies (~2140 to 2100 Ma) (Hirdes et al., 1996; Liégeois et al., 1991; Masurel et al., 2017; Tshibubudze et al., 2015; Wane et al., 2018).

Metamorphism is typically characterized by regional greenschist facies conditions (Hirdes et al., 1992; Křibek et al., 2008; Taylor et al., 1992), but locally reaches amphibolite facies or even granulite facies metamorphism (Block et al., 2015; Ganne et al., 2014; John et al., 1999; Pons et al., 1995; Soumaila and Garba, 2006).

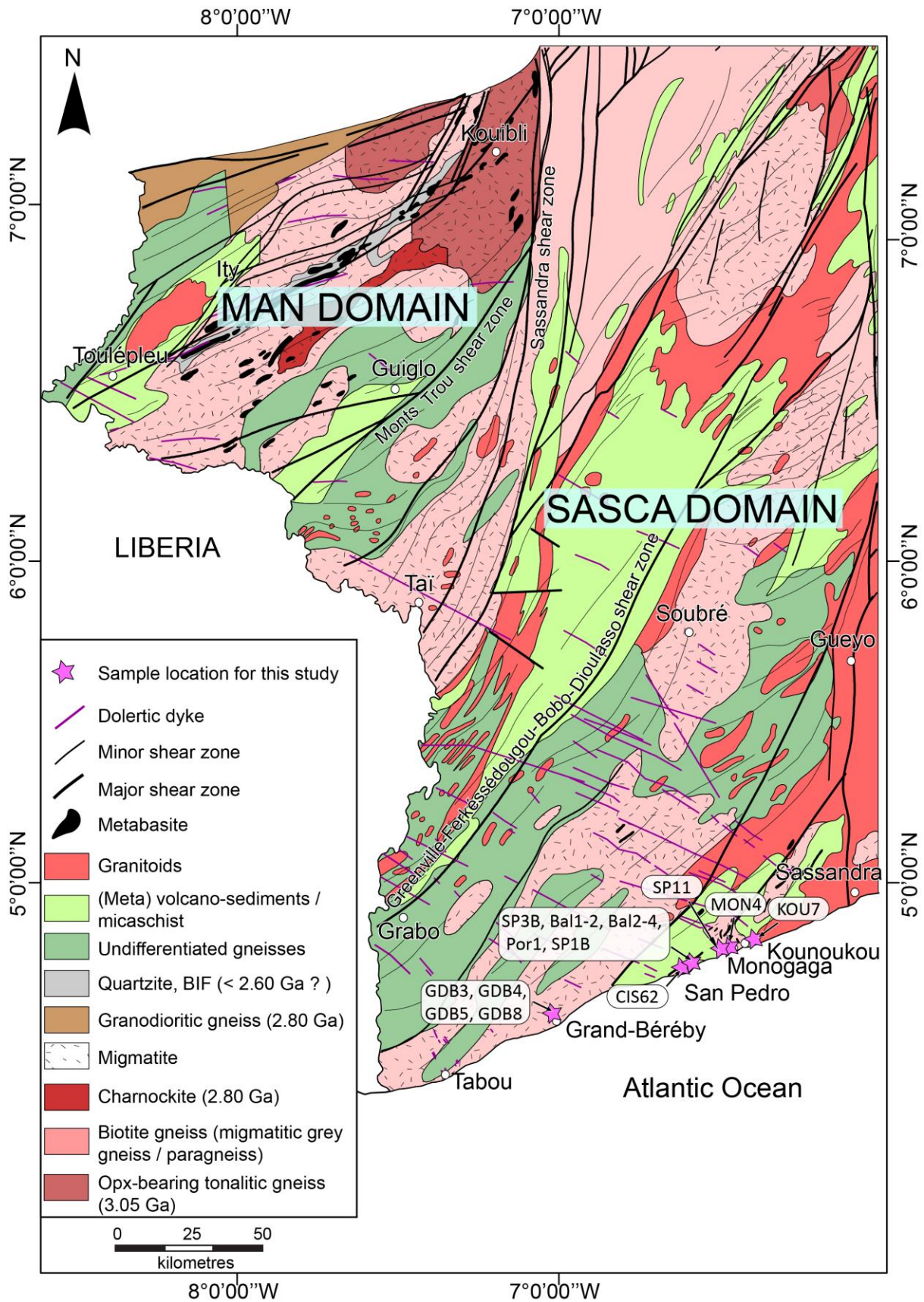


**Fig. 2.** Litho-structural map of the SW of Côte d'Ivoire, modified after (Papon, 1973; Pitra et al., 2010; Tagini, 1971; WAXI report, AMIRA Global, 2018). Purple stars show the location of the studied rocks of the SASCA domain.

### 3. GEOLOGY OF THE SASSANDRA-CAVALLY DOMAIN

The SASCA domain located at the border between Côte d'Ivoire and Liberia consists of Archean metamorphic and granitic basement rocks overlain by Birimian pelitic formations interlayered with acid and basic tuffs (Papon, 1973). Sm-Nd whole rock model ages of ca. 3450 Ma have been obtained on migmatitic gneiss of San Pedro, and ca. 2400 Ma on metapelitic schists at Kounoukou. The presence of Archean crustal relics has been confirmed by a U-Pb zircon age of  $3207 \pm 7$  Ma (Kouamelan et al., 2015). Based on the study of the coastal section between Grand-Béréby and Sassandra by Koffi (2019), polyphase deformation was documented in the SASCA domain. The first deformation phase is characterized by a NW-SE-oriented subvertical penetrative metamorphic foliation  $S_1$  with occasional synfolial rootless folds. The  $S_1$  is affected by open  $F_2$  folds with shallow NNE-plunging axes and by dominantly sinistral ductile NNE-SSW trending shear-zones. At San Pedro, the shear zones locally crosscut the fold limbs. The presence of leucosome and pegmatite veins concordant to the  $S_1$  and  $S_2$  foliation planes, as well as in axial planes of  $F_2$  folds or in shear zones, indicates that deformation occurred in the presence of melt, which in turn promoted melt segregation (**Fig. 3**). The migmatitic gneiss comprises veins of granite discordant to  $S_2$  but in a structural position similar to discordant leucosome suggesting an origin by segregation of partial melts from the migmatitic gneiss. The  $L_2$  mineral lineation plunges between  $80^\circ$  and  $30^\circ$  to the NNE. Open  $F_3$  folds with W-plunging axes and a penetrative subvertical E-W axial planar schistosity  $S_3$  affect the  $S_1$  and  $S_2$  foliations. In Monogaga, the  $F_3$  folds with E-W axial planes overprint the  $F_2$ , leading to hook-shape fold interference patterns. In the San Pedro area, discrete E-W-striking dextral shear-zones  $S_4$  are localized along the contact between a potassic granite and the migmatitic gneisses (**Fig. 3c**, Koffi, 2019).

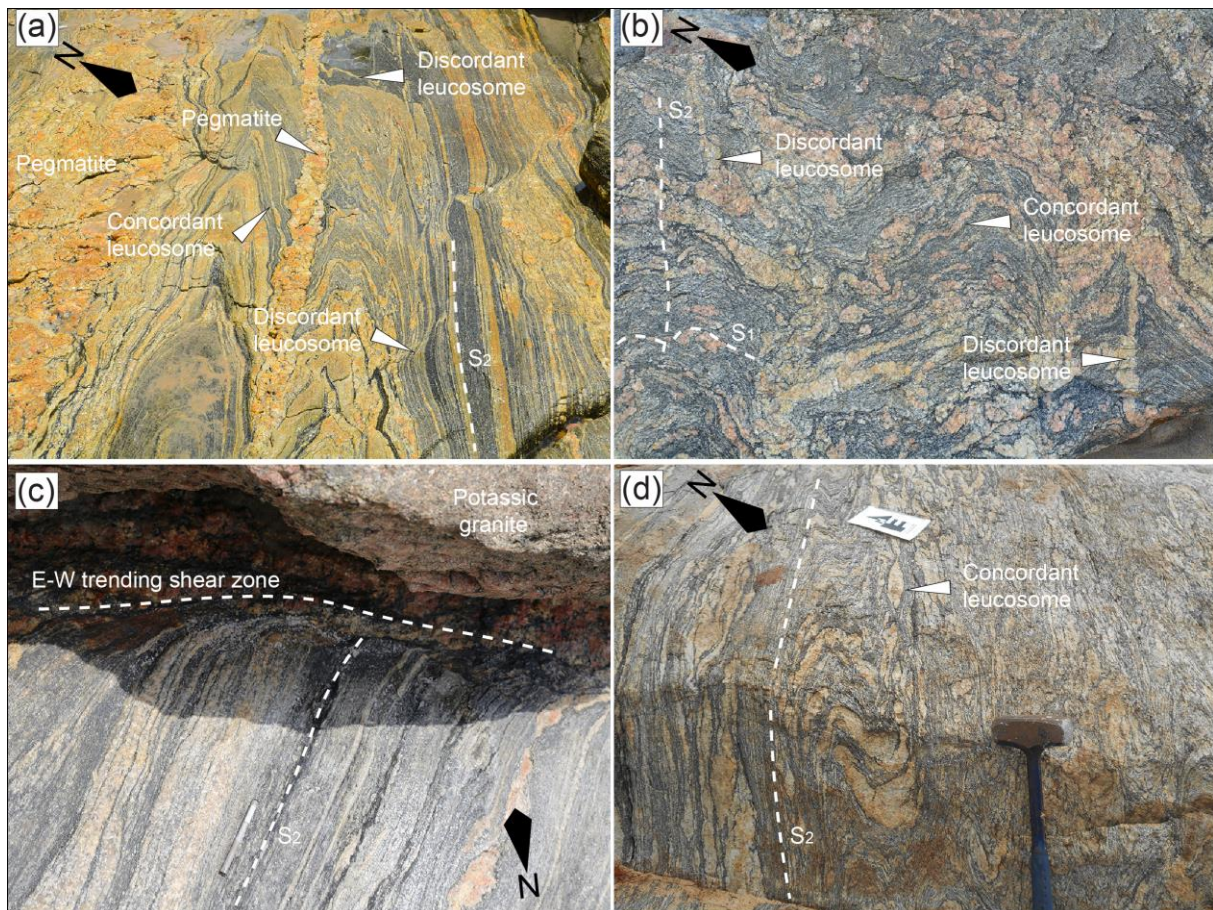


**Fig. 3.** Leucosome veins concordant or discordant to the  $S_2$  foliation in the San Pedro migmatitic gneisses (a, b and c) and Grand-Béréby (d). Potassic granite intersects the  $S_2$  foliation and is emplaced along the E-W oriented shear zones (c).

#### 4. ANALYTICAL METHODS

Thirteen samples were collected for this study in the Sassandra-Cavally domain at San Pedro along a coastal transect, which covers the zone of transition (Sassandra shear zone) between the Archean and Paleoproterozoic metamorphic and magmatic units: (migmatitic gneisses and potassic granite: 5 and 1 samples, respectively), Monogaga (migmatitic gneisses, 2 samples), Grand-Béréby (garnet-cordierite-sillimanite migmatitic gneiss, 4 samples), and Kounoukou (garnet-staurolite-bearing micaschist, 1 sample). Only a representative subset of these samples was analysed for geochronology (SP3B, SP11, MON4, GDB8, KOU7, CIS62) (**Fig. 2**).

##### 4.1 Geochemical characterisation

Whole rock major and trace elements were analysed in 13 samples (SP3B, Bal1-2, Bal2-4, Por1, SP1B, SP11, MON4, GDB3, GDB4, GDB5, GDB8, KOU7 and CIS62) at Actlabs in Ancaster (Canada) (Table 1). Samples were digested by lithium metaborate and tetraborate fusion. Major

and trace elements analyses were achieved by ICP-OES and ICP-MS, respectively (**Table 1**). Fe is measured as total Fe<sub>2</sub>O<sub>3</sub>. In the multi-element diagrams, the abundances were normalized with respect to primitive-mantle and chondrites according to the values established by McDonough et al. (1992) and Sun and McDonough (1989), respectively.

## 4.2 Radiogenic isotopic geochemistry

Six of the samples characterised by geochemistry (SP3B, GDB8, KOU7, CIS62, SP11 and MON4) were further analysed for zircon U-Pb and Lu-Hf by Laser Ablation-Inductively Coupled Plasma-Mass Spectrometry (LA-ICPMS). The description of the analytical methods applied is presented in supplementary materials and the acquired data are provided in Table 2.

**Table 1:** Whole rock major and trace element composition.

| Sample                         | MGSP <sup>a</sup> |         |         |         |         | MGM <sup>a</sup> |         | GCSMGGB <sup>a</sup> |         |         |         | GSMK <sup>a</sup> | PGSP <sup>a</sup> | DL <sup>b</sup> |
|--------------------------------|-------------------|---------|---------|---------|---------|------------------|---------|----------------------|---------|---------|---------|-------------------|-------------------|-----------------|
|                                | SP3B              | Bal 1-2 | Bal 2-4 | Por 1   | SP 1B   | SP 11            | MON4    | GDB8                 | GDB3    | GDB4    | GDB5    | CIS63             | CIS62             |                 |
| WGS 84 coordinate system       |                   |         |         |         |         |                  |         |                      |         |         |         |                   |                   |                 |
| Lat <sup>c</sup>               | 4.72295           | 4.72076 | 4.72299 | 4.74307 | 4.73089 | 4.79892          | 4.80868 | 4.72122              | 4.64294 | 4.65084 | 4.64521 | 4.82163           | 4.72084           |                 |
| Long <sup>c</sup>              | -6.6395           | -6.6508 | -6.6392 | -6.6199 | -6.6389 | -6.4423          | -6.441  | -6.9533              | -6.9174 | -6.9202 | -6.9166 | -6.3978           | -6.6504           |                 |
| wt% <sup>d</sup>               |                   |         |         |         |         |                  |         |                      |         |         |         |                   |                   |                 |
| SiO <sub>2</sub>               | 68.89             | 64.90   | 71.20   | 67.80   | 68.90   | 66.70            | 55.90   | 56.40                | 63.30   | 65.00   | 61.90   | 63.00             | 78.86             | 0.01            |
| TiO <sub>2</sub>               | 0.48              | 0.57    | 0.34    | 0.42    | 0.38    | 0.47             | 0.46    | 0.99                 | 0.85    | 0.72    | 0.68    | 0.69              | 0.059             | 0.001           |
| Al <sub>2</sub> O <sub>3</sub> | 15.09             | 16.30   | 13.80   | 15.90   | 15.70   | 15.30            | 14.40   | 19.60                | 18.10   | 17.50   | 15.20   | 17.90             | 11.51             | 0.01            |
| Fe <sub>2</sub> O <sub>3</sub> | 4.48              | 5.62    | 3.87    | 4.51    | 3.51    | 4.65             | 10.40   | 10.40                | 8.98    | 8.41    | 9.84    | 8.16              | 1.01              | 0.01            |
| MnO                            | 0.069             | 0.08    | 0.04    | 0.06    | 0.05    | 0.05             | 0.19    | 0.12                 | 0.09    | 0.09    | 0.13    | 0.07              | 0.007             | 0.001           |
| MgO                            | 1.3               | 1.77    | 2.30    | 1.19    | 1.54    | 2.25             | 5.32    | 3.92                 | 2.70    | 2.15    | 3.13    | 2.73              | 0.25              | 0.01            |
| CaO                            | 2.73              | 4.05    | 1.88    | 4.05    | 2.83    | 3.12             | 8.62    | 1.97                 | 1.25    | 1.35    | 2.58    | 1.88              | 0.33              | 0.01            |
| Na <sub>2</sub> O              | 4.07              | 3.93    | 3.88    | 3.82    | 4.87    | 4.07             | 3.48    | 3.19                 | 1.97    | 2.23    | 3.08    | 2.41              | 2.41              | 0.01            |
| K <sub>2</sub> O               | 1.63              | 1.83    | 2.05    | 1.44    | 1.72    | 2.20             | 0.77    | 2.20                 | 2.12    | 1.94    | 2.24    | 2.09              | 5.53              | 0.01            |
| P <sub>2</sub> O <sub>5</sub>  | 0.17              | 0.22    | 0.02    | 0.18    | 0.14    | 0.19             | 0.05    | 0.08                 | 0.05    | 0.06    | 0.22    | 0.13              | 0.05              | 0.01            |
| LOI                            | 1.42              | 0.09    | 0.40    | 0.18    | 0.11    | 0.30             | 0.35    | 0.41                 | 0.12    | 0.09    | 0.37    | 0.47              | 0.72              | 0.01            |
| Total                          | 100.3             | 99.36   | 99.78   | 99.55   | 99.75   | 99.30            | 99.94   | 99.28                | 99.53   | 99.54   | 99.37   | 99.53             | 100.7             | 0.01            |
| ppm <sup>d</sup>               |                   |         |         |         |         |                  |         |                      |         |         |         |                   |                   |                 |
| Cs                             | 2.8               | 3.30    | 1.80    | 0.70    | 2.10    | 0.40             | 0.09    | 2.30                 | 1.50    | 0.90    | 3.00    | 8.50              | 0.8               | 0.1             |
| Rb                             | 91                | 98.20   | 90.60   | 55.10   | 73.70   | 121.60           | 4.50    | 172.80               | 99.50   | 116.50  | 132.90  | 75.20             | 106               | 1               |
| Ba                             | 239               | 286.00  | 375.00  | 439.00  | 159.00  | 369.00           | 114.00  | 357.00               | 575.00  | 271.00  | 367.00  | 679.00            | 748               | 2               |
| Th                             | 24.1              | 16.50   | 19.10   | 9.10    | 16.10   | 13.90            | 2.10    | 7.70                 | 7.80    | 7.70    | 5.90    | 4.10              | 8.57              | 0.05            |
| Nb                             | 13.2              | 17.40   | 6.00    | 8.90    | 10.20   | 10.00            | 3.20    | 12.30                | 7.90    | 7.60    | 7.70    | 5.90              | 1.8               | 0.2             |
| Pb                             | 25                | 5.10    | 3.20    | 2.30    | 3.80    | 2.10             | 1.60    | 2.60                 | 1.60    | 2.00    | 3.50    | 1.60              | 39                | 0.1             |
| Sr                             | 235               | 330.20  | 424.70  | 328.40  | 234.10  | 301.70           | 126.90  | 237.00               | 242.00  | 173.20  | 273.60  | 269.30            | 168               | 2               |
| Zr                             | 241               | 220.90  | 193.50  | 240.80  | 199.00  | 117.30           | 92.30   | 162.80               | 214.00  | 158.40  | 226.80  | 121.40            | 12                | 1               |
| Y                              | 20.8              | 22.60   | 4.40    | 12.00   | 13.00   | 8.70             | 16.60   | 18.20                | 24.10   | 22.60   | 34.20   | 18.60             | 22                | 0.5             |
| V                              | 47                | 77.00   | 34.00   | 37.00   | 51.00   | 63.00            | 157.00  | 175.00               | 144.00  | 126.00  | 111.00  | 145.00            | 6                 | 5               |
| Ni                             | 19.9              | 16.80   | 6.30    | 7.20    | 6.50    | 30.80            | 35.60   | 92.70                | 71.40   | 61.50   | 53.00   | 53.60             | < 20              | 0.1             |
| Hf                             | 5.4               | 5.60    | 5.10    | 5.10    | 4.80    | 3.00             | 2.40    | 4.60                 | 5.90    | 4.40    | 5.80    | 3.40              | 0.3               | 0.1             |
| Sn                             | 3                 | 3.00    | 2.00    | 1.00    | 2.00    | 2.00             | 1.00    | 4.00                 | 2.00    | 2.00    | 1.00    | 0.90              | < 1               | 1               |
| Ta                             | 2.72              | 2.40    | 0.30    | 0.60    | 0.80    | 0.40             | 0.40    | 0.90                 | 0.40    | 0.40    | 0.90    | 0.50              | 0.12              | 0.01            |
| U                              | 3.59              | 3.70    | 1.50    | 2.70    | 2.60    | 0.40             | 0.90    | 2.00                 | 0.80    | 1.60    | 2.10    | 1.30              | 1.43              | 0.01            |
| W                              | 0.49              | 0.49    | 0.49    | 0.49    | 0.49    | 0.49             | 0.49    | 0.49                 | 0.49    | 0.49    | 0.70    | 0.49              | 2.2               | 0.5             |
| La                             | 67.5              | 43.90   | 41.00   | 36.50   | 37.60   | 36.90            | 13.00   | 31.30                | 36.30   | 32.80   | 25.00   | 22.00             | 10.8              | 0.05            |
| Ce                             | 120               | 79.10   | 69.40   | 62.70   | 62.50   | 66.60            | 20.20   | 66.00                | 76.30   | 67.80   | 51.30   | 45.10             | 20.3              | 0.05            |
| Pr                             | 12.4              | 8.99    | 6.64    | 5.71    | 6.49    | 6.94             | 2.51    | 7.20                 | 8.53    | 7.59    | 5.88    | 5.50              | 2.1               | 0.01            |
| Nd                             | 42.1              | 30.70   | 21.50   | 17.80   | 21.10   | 23.50            | 9.90    | 28.00                | 32.10   | 29.00   | 23.80   | 20.60             | 7.62              | 0.05            |
| Sm                             | 6.98              | 5.24    | 2.82    | 2.81    | 3.49    | 4.09             | 2.25    | 5.02                 | 6.03    | 5.51    | 4.82    | 4.12              | 1.79              | 0.01            |
| Eu                             | 1.29              | 1.19    | 0.73    | 0.89    | 0.86    | 0.82             | 0.84    | 1.26                 | 1.31    | 1.19    | 1.31    | 1.03              | 0.51              | 0.005           |
| Gd                             | 5.53              | 4.37    | 1.92    | 2.54    | 3.10    | 3.12             | 2.72    | 4.36                 | 5.41    | 4.70    | 5.75    | 3.90              | 2.23              | 0.01            |
| Tb                             | 0.76              | 0.63    | 0.19    | 0.34    | 0.43    | 0.38             | 0.47    | 0.65                 | 0.80    | 0.72    | 1.00    | 0.57              | 0.45              | 0.01            |
| Dy                             | 3.99              | 3.74    | 0.89    | 2.08    | 2.48    | 1.91             | 3.01    | 3.54                 | 4.34    | 4.05    | 6.26    | 3.31              | 2.98              | 0.05            |

|                                    |         |         |         |         |         |         |         |         |         |         |         |         |         |       |
|------------------------------------|---------|---------|---------|---------|---------|---------|---------|---------|---------|---------|---------|---------|---------|-------|
| Ho                                 | 0.7     | 0.73    | 0.13    | 0.40    | 0.44    | 0.29    | 0.60    | 0.69    | 0.93    | 0.85    | 1.41    | 0.66    | 0.67    | 0.01  |
| Er                                 | 1.94    | 2.24    | 0.35    | 1.23    | 1.24    | 0.73    | 1.87    | 1.97    | 2.73    | 2.69    | 3.99    | 1.93    | 2.12    | 0.01  |
| Tm                                 | 0.278   | 0.35    | 0.05    | 0.18    | 0.18    | 0.10    | 0.26    | 0.24    | 0.38    | 0.39    | 0.55    | 0.29    | 0.312   | 0.005 |
| Yb                                 | 1.75    | 2.50    | 0.41    | 1.18    | 1.11    | 0.55    | 1.80    | 1.58    | 2.58    | 2.56    | 3.77    | 1.93    | 1.89    | 0.01  |
| Lu                                 | 0.29    | 0.40    | 0.08    | 0.21    | 0.17    | 0.09    | 0.27    | 0.23    | 0.39    | 0.38    | 0.56    | 0.29    | 0.288   | 0.002 |
| Tl                                 | 0.47    | 0.50    | 0.40    | 0.30    | 0.40    | 0.60    | 0.09    | 0.80    | 0.40    | 0.60    | 0.60    | 0.30    | 0.5     | 0.05  |
| A/CNK                              | 1.12    | 1.03    | 1.15    | 1.04    | 1.04    | 1.04    | 0.65    | 1.75    | 2.32    | 2.13    | 1.25    | 1.85    | 1.09    |       |
| A/NK                               | 1.78    | 1.93    | 1.60    | 2.03    | 1.59    | 1.68    | 2.19    | 2.57    | 3.27    | 3.03    | 2.03    | 2.87    | 1.15    |       |
| Eu/Eu*                             | 0.64    | 0.77    | 0.97    | 1.03    | 0.81    | 0.71    | 1.05    | 0.83    | 0.71    | 0.72    | 0.77    | 0.79    | 0.79    |       |
| (La/Yb) <sub>N</sub>               | 25.41   | 11.57   | 65.87   | 20.38   | 22.31   | 44.19   | 4.76    | 13.05   | 9.27    | 8.44    | 4.37    | 7.51    | 3.76    |       |
| (Gd/Yb) <sub>N</sub>               | 2.53    | 1.40    | 3.75    | 1.72    | 2.24    | 4.54    | 1.21    | 2.21    | 1.68    | 1.47    | 1.22    | 1.62    | 0.94    |       |
| K <sub>2</sub> O/Na <sub>2</sub> O | 0.40049 | 0.46565 | 0.52835 | 0.37696 | 0.35318 | 0.54054 | 0.22126 | 0.68966 | 1.07614 | 0.86996 | 0.72727 | 0.86722 | 2.29461 |       |
| Sr/Y                               | 11.2981 | 14.6106 | 96.5227 | 27.3667 | 18.0077 | 34.6782 | 7.64458 | 13.022  | 10.0415 | 7.66372 | 8       | 14.4785 | 7.63636 |       |

(a) MGSP: Migmatitic gneiss of San Pedro, MGM: Migmatitic gneiss of Monogaga, GCSMGGGB: Garnet-cordierite-sillimanite migmatitic gneiss of Grand-Béréby, GSMK: Garnet-staurolite-bearing micaschist of Kounoukou, PGSP: Potassic granite of San Pedro. (b) DL: Detection Limit. (c) Latitude-Longitude of the sample in the WGS84 coordinate system. (d) major element in wt% and trace elements in ppm.

## 5. RESULTS

### 5.1. Petrographic characteristics

#### *- Migmatitic gneisses of San Pedro*

Macroscopically, the rocks are banded grey migmatitic gneisses. The sample SP3B comprises quartz (40%), plagioclase (35%), greenish biotite (20%) and garnet (3%). Monazite, ilmenite, magnetite and zircon are the main accessory minerals. The foliation is marked by alternating quartzo-feldspathic and biotite-rich layers, several mm up to 1 cm thick. Locally, significantly coarser-grained quartzo-feldspathic leucosomes, up to 10 cm thick, are present with a spacing of 20-50 cm. Leucosomes are forming a continuous network from veins concordant with the S<sub>1</sub> foliation to veins parallel to the axial planar S<sub>2</sub> foliation but may also be localised in necks of foliation boudins (**Figs. 3a, b, c and 4a**). E-W trending subvertical shear bands S<sub>4</sub> cross-cut the NE-trending foliation S<sub>2</sub>. Greenish biotite is aligned parallel to the S<sub>2</sub> foliation but also commonly crystallizes around garnet. Monazite typically forms crystal aggregates in the leucosome, aligned parallel to the foliation S<sub>2</sub> and locally occurs as inclusions in garnet. Numerous grains of zircon are included in biotite, feldspar and garnet.

#### *- Migmatitic gneisses of Monogaga*

Macroscopically, the sample SP11 is a grey migmatitic gneiss. This rock comprises medium to coarse-grained plagioclase (40%), quartz (35%), greenish biotite (20%), greenish hornblende (2%) and locally minor garnet (**Fig. 4b**). Zircon and ilmenite are the main accessory minerals. The syn-migmatitic foliation S<sub>2</sub> is marked by alternating quartzo-feldspathic and biotite-rich

layers including rare greenish hornblende, representing leucosomes and mesosomes, several mm up to 1 cm thick. Biotite flakes show preferred orientation parallel to S<sub>2</sub>.

Sample MON4, collected at ca. 500 meters to the east of SP11, is also a grey, medium to coarse grained (up to 5 mm) migmatitic gneiss. It consists of hornblende (40%), plagioclase (30%), quartz (25%) and K-feldspar (3%). Epidote, zircon, ilmenite and magnetite are the main accessory minerals. The foliation S<sub>2</sub> is marked by hornblende-rich and quartz-feldspar-rich layers with thicknesses ranging from several mm to up to 1 cm (**Fig. 4c**).

*- Garnet-cordierite-sillimanite migmatitic gneiss of Grand-Béréby*

Macroscopically, the gneiss of Grand-Béréby (GDB8) displays a prominent migmatitic texture with coarse-grained quartzo-feldspathic leucosome layers (1-10 cm thick), rimmed by thin layers of biotite-rich melanosome, and alternating with layers of mesosome. The mineralogy of the mesosome consists of biotite (35%), quartz (30%), plagioclase (25%), sillimanite (5%), garnet (3%) and cordierite (2%). Zircon, ilmenite, magnetite and hematite are the main accessory minerals. Biotite and sillimanite show preferred orientation along the foliation S<sub>2</sub> which wraps around anhedral porphyroblasts of garnet (up to 2.5 mm). Garnet is commonly surrounded by cordierite and locally replaced by symplectitic intergrowths of biotite and quartz. (**Fig. 4d**). The mineral assemblages of the mesosomes suggests a sedimentary, pelitic protolith.

*- Garnet-staurolite-bearing micaschist of Kounoukou*

A macroscopically dark-colored micaschist from Kounoukou (KOU7) consists of quartz (35%), biotite (35%), plagioclase (15%), garnet (5%) and staurolite (5%). Zircon, ilmenite and tourmaline are the main accessory minerals. Garnet and staurolite form porphyroblasts (up to 3 mm) in a matrix dominated by quartz and plagioclase. Biotite, commonly altered to chlorite, marks the foliation S<sub>3</sub>. Subhedral garnet contains abundant inclusions of quartz. Poikiloblastic staurolite contains abundant quartz inclusions. (**Fig. 4e**). The mineral assemblage with the preserved sedimentary bedding suggests a sedimentary, pelitic protolith.

*- Potassic granite of San Pedro*

The potassic granite (CIS62) intrudes the migmatitic grey gneiss of San Pedro. The mineralogy consists of quartz (35%), plagioclase (25%), K-feldspar (25%), biotite (10%) and muscovite (5%). Plagioclase occurs both as phenocrysts and in the groundmass. K-feldspar is microcline, commonly displays a cloudy appearance and is locally overgrown by muscovite (**Fig. 4f**).

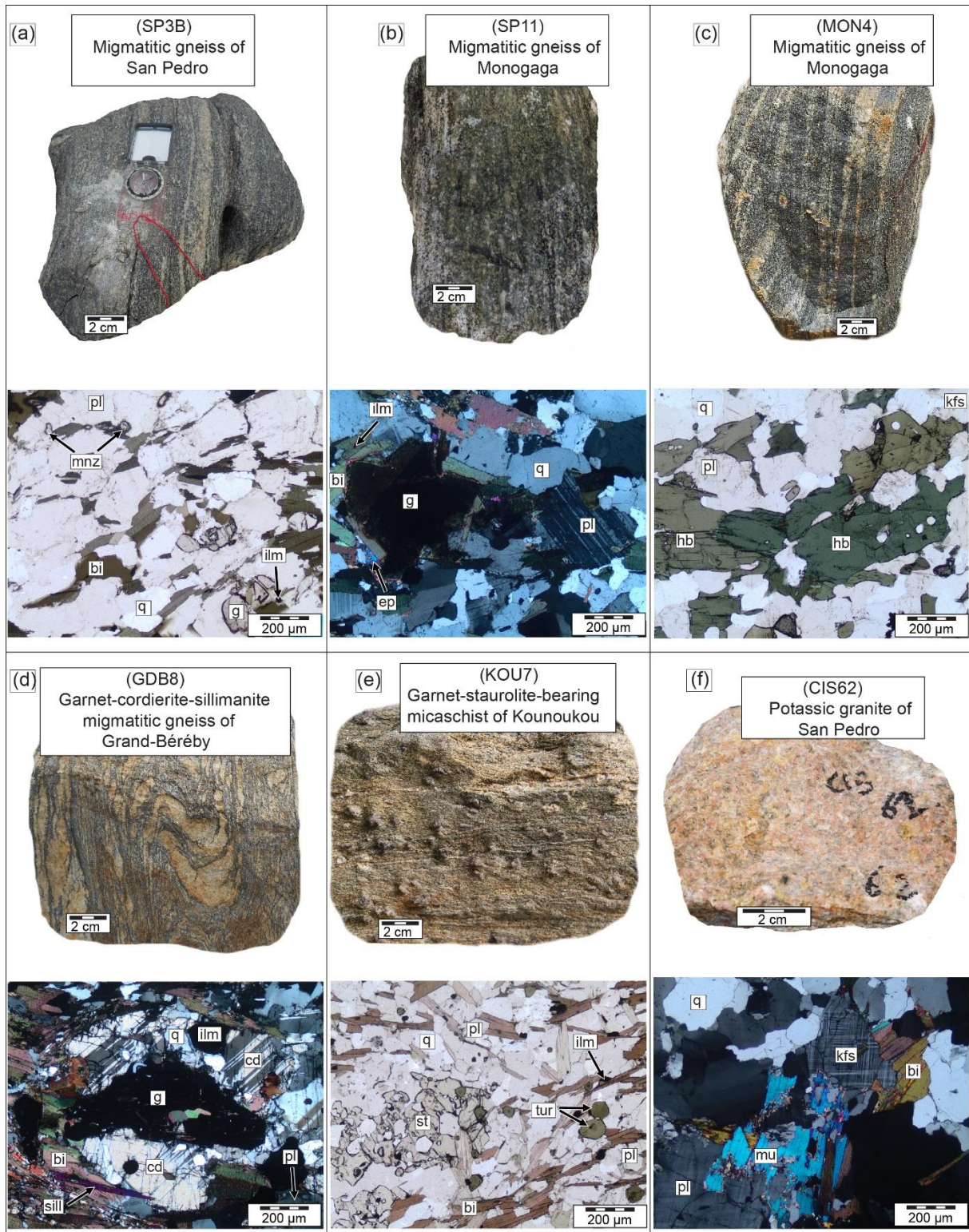


**Fig. 4.** Photographs and microphotographs showing the studied rocks of the Sassandra-Cavally domain. Abbreviations: q = quartz; pl = plagioclase; bi = biotite; g = garnet; kfs = K-feldspar; mu = muscovite; mnz = monazite, sill = sillimanite, tur = tourmaline, hb = hornblende, st = staurolite, cd = cordierite, ep = epidote and ilm = ilmenite.

## 5.2. Geochemical characteristics

### - Migmatitic gneisses of San Pedro

The migmatitic gneisses of San Pedro (orange squares, **Fig. 5a**) are characterized by relatively high SiO<sub>2</sub> (64.9–71.2 wt%), Al<sub>2</sub>O<sub>3</sub> (13.8–16.3 wt%) and Na<sub>2</sub>O (3.8–4.9 wt%). These migmatitic gneisses are also characterized by low MgO (1.2–2.3 wt%), TiO<sub>2</sub> (0.3–0.6 wt%), and Fe<sub>2</sub>O<sub>3</sub> (3.5–5.6 wt%) compared to other samples, while CaO (1.9–4.1 wt%), K<sub>2</sub>O (1.4–2.1 wt%) and P<sub>2</sub>O<sub>5</sub> (0.02–0.2 wt%) show comparable values. They are slightly peraluminous (A/CNK = 1.04–1.15 and A/NK = 1.59–2.03) (**Fig. 5b**) with the K<sub>2</sub>O/Na<sub>2</sub>O comprised between 0.35 and 0.53. The Sr/Y ratio is comprised between 11.3 and 27.4, with the exception of sample Bal 2-4, which shows anomalously high values (96.5) (**Fig. 4c**). In a normative An-Ab-Or classification diagram (O'Connor, 1965), migmatitic gneisses correspond to granodiorite (three samples), trondhjemite (one sample), and granite (one sample) (**Fig. 5d**). The ternary diagram Al<sub>2</sub>O<sub>3</sub>/(FeO<sub>t</sub> + MgO); 3 \* CaO; 5 \* (K<sub>2</sub>O/Na<sub>2</sub>O) proposed by Laurent et al. (2014) defines a magmatic source ranging from high-K to low-K mafic rocks (**Fig. 5e**). The migmatitic gneisses of San Pedro are enriched in lithophile elements (LILE) (Rb, Th, U) and overall yield positive Th anomalies and negative K, Nb and Ti anomalies (**Fig. 6**). The gneisses are enriched in light Rare-Earth Elements (LREE) and display La<sub>N</sub>/Yb<sub>N</sub> = 11.6–65.9, and Gd<sub>N</sub>/Yb<sub>N</sub> = 1.4–3.8.

### - Migmatitic gneisses of Monogaga

Sample SP11 (light purple ellipse, **Fig. 5a**) shows higher SiO<sub>2</sub> (66.7 wt%) than migmatitic gneiss of Monogaga MON4 (light blue diamond, SiO<sub>2</sub> = 55.9 wt%). Values of Al<sub>2</sub>O<sub>3</sub>, Na<sub>2</sub>O and TiO<sub>2</sub> of SP11 (15.3, 4.1 and 0.5 wt%) are essentially the same as MON4 (14.4, 3.5 and 0.5 wt%). In contrast, Fe<sub>2</sub>O<sub>3</sub>, MgO and CaO of MON4 (10.4, 5.3 and 8.6 wt%) are higher than those of SP11 (4.7, 2.3 and 3.1 wt%) while K<sub>2</sub>O and P<sub>2</sub>O<sub>5</sub> are lower in MON4 (0.8 and 0.1 wt%) than in SP11 (2.2 and 0.2 wt%) (**Fig. 5a**). MON4 is metaluminous (A/CNK = 0.7 and A/NK = 1.7) with Sr/Y = 7.6 and K<sub>2</sub>O/Na<sub>2</sub>O = 0.2 values while SP11 is slightly peraluminous (A/CNK = 1.0 and A/NK = 2.2) (**Fig. 5b**), with Sr/Y = 34.7 and K<sub>2</sub>O/Na<sub>2</sub>O = 0.5 values (**Fig. 5c**). In a normative An-Ab-Or classification diagram (O'Connor, 1965), migmatitic gneisses of Monogaga correspond to a tonalite and a grandiorite (**Fig. 5d**). The diagram of Laurent et al. (2014) defines a magmatic source for the Monogaga migmatitic gneisses close the boundary of the high-K to low-K mafic rocks (**Fig. 5e**). The migmatitic gneisses of Monogaga are enriched in light Rare-Earth Elements (LREE) with MON4 (La<sub>N</sub>/Yb<sub>N</sub> = 4.8, Gd<sub>N</sub>/Yb<sub>N</sub> = 1.2) less fractionated in LREE than SP11 (La<sub>N</sub>/Yb<sub>N</sub> = 44.2, Gd<sub>N</sub>/Yb<sub>N</sub> = 4.5). MON4 has a very slightly positive (1.1) and SP11 displays a weak negative (0.7) Eu/Eu\* anomaly. Both samples are

enriched in lithophile elements (LILE) (Rb, Th, U) and are marked overall by positive Th anomalies and negative K, Nb and Ti as well as a slight negative Ta anomaly in SP11 (**Fig. 6**).

- *Garnet-cordierite-sillimanite migmatitic gneiss of Grand-Béréby*

The garnet-cordierite-sillimanite migmatitic gneisses of Grand-Béréby (yellow stars, **Fig. 5a**) display intermediate to high SiO<sub>2</sub> (56.4–65.0 wt%), relatively high Al<sub>2</sub>O<sub>3</sub> (15.2–19.6 wt%), Fe<sub>2</sub>O<sub>3</sub> (8.4–10.4 wt%), TiO<sub>2</sub> (0.7–1.0 wt%) and relatively low MgO (2.2–3.9 wt%), Na<sub>2</sub>O (2.0–3.2 wt%), CaO (1.3–2.6 wt%), K<sub>2</sub>O (2.0–2.2 wt%), P<sub>2</sub>O<sub>5</sub> (0.05–0.2 wt%). They are strongly peraluminous (A/CNK = 1.3–2.3 and A/NK = 2.0–3.3) (**Fig. 5b**). Sr/Y varies between 7.7 and 13, K<sub>2</sub>O/Na<sub>2</sub>O is comprised between 0.7 and 1.1 (**Fig. 5c**). The source of the garnet-cordierite-sillimanite migmatitic gneiss of Grand-Béréby defines a trend to the metasediments field (**Fig. 5e**). The garnet-cordierite-sillimanite migmatitic gneisses of Grand-Béréby are enriched in LREE and show relatively flat HREE patterns (La<sub>N</sub>/Yb<sub>N</sub> = 4.4–13.1, Gd<sub>N</sub>/Yb<sub>N</sub> = 1.2–2.2) with weak negative Eu anomalies (Eu/Eu\* = 0.7–0.8) (**Fig. 6**). They have incompatible trace element patterns characterized by enrichment in LILE such as Rb, Ba and U. They display positive La, Th and Ce and negative Sr, K, Ta and Ti anomalies (**Fig. 6**). In the ternary diagram Al<sub>2</sub>O<sub>3</sub>/(FeO<sub>t</sub> + MgO); 3 \* CaO; 5 \* (K<sub>2</sub>O/Na<sub>2</sub>O) proposed by [Laurent et al. \(2014\)](#), the Grand-Béréby samples are clearly distinct from the migmatitic gneisses of San Pedro and Monogaga and they fall in the field of sedimentary source and high-K mafic rocks source, due to their higher K<sub>2</sub>O/Na<sub>2</sub>O ratio (**Fig. 5e**).

- *Garnet-staurolite-bearing micaschist of Kounoukou*

Garnet-staurolite-bearing micaschist of Kounoukou (light green polygone, **Fig. 5a**) shows relatively high SiO<sub>2</sub> (63.0 wt%), Al<sub>2</sub>O<sub>3</sub> (17.9 wt%) and Fe<sub>2</sub>O<sub>3</sub> (8.2 wt%). This rock is also characterized by low MgO (2.7 wt%), Na<sub>2</sub>O (2.4 wt%), TiO<sub>2</sub> (0.7 wt%), CaO (1.9 wt%), K<sub>2</sub>O (2.1 wt%) and P<sub>2</sub>O<sub>5</sub> (0.1 wt%). The rock is strongly peraluminous (A/CNK = 1.9 and A/NK = 2.9) (**Fig. 5 and 5b**) with Sr/Y = 14.5 and K<sub>2</sub>O/Na<sub>2</sub>O = 0.9 (**Fig. 5c**). The source of the garnet-staurolite-bearing micaschist of Kounoukou defines a trend to the metasediments field (**Fig. 5e**). The garnet-staurolite-bearing micaschist is enriched in LREE and shows relatively flat HREE patterns (La<sub>N</sub>/Yb<sub>N</sub> = 7.5, Gd<sub>N</sub>/Yb<sub>N</sub> = 1.6) with weak negative Eu anomalies (Eu/Eu\* = 0.8) (**Fig. 6**). This garnet-staurolite-bearing micaschist has incompatible trace element patterns characterized by enrichment in LILE such as Rb, Ba and U. It displays positive La and Ce and negative Sr, K, Nb, Ta and Ti anomalies (**Fig. 6**). In the ternary diagram Al<sub>2</sub>O<sub>3</sub>/(FeO<sub>t</sub> + MgO);

3 \* CaO; 5 \* (K<sub>2</sub>O/Na<sub>2</sub>O) proposed by [Laurent et al. \(2014\)](#), the Kounoukou micaschist falls at the boundary between the sedimentary and high-K mafic rocks source (**Fig. 5e**).

*- Potassic granite of San Pedro*

The potassic granite of San Pedro (light orange triangle, **Fig. 5a**) shows high SiO<sub>2</sub> (78.9 wt%) and K<sub>2</sub>O (5.5 wt%), relatively low Al<sub>2</sub>O<sub>3</sub> (11.5 wt%), MgO (0.3 wt%), Na<sub>2</sub>O (2.4 wt%), TiO<sub>2</sub> (0.1 wt%), Fe<sub>2</sub>O<sub>3</sub> (1.0 wt%), CaO (0.3 wt%), and P<sub>2</sub>O<sub>5</sub> (0.1 wt%). This potassic granite is slightly peraluminous (A/CNK = 1.1 and A/NK = 1.2) (**Fig. 5a** and **5b**) with Sr/Y = 7.6 and K<sub>2</sub>O/Na<sub>2</sub>O = 2.3 (**Fig. 5c**). The granite is enriched in LREE and displays a flat HREE pattern (La<sub>N</sub>/Yb<sub>N</sub> = 3.8, Gd<sub>N</sub>/Yb<sub>N</sub> = 0.9) and a negative Eu anomaly (Eu/Eu\* = 0.8). The analyzed sample is characterized by an enrichment in LILE and negative Nb and Ti anomalies (**Fig. 6**). In a normative An-Ab-Or classification diagram ([O'Connor, 1965](#)), the potassic granite corresponds to a granite. (**Fig. 5d**). The ternary diagram Al<sub>2</sub>O<sub>3</sub>/(FeO<sub>t</sub> + MgO); 3 \* CaO; 5 \* (K<sub>2</sub>O/Na<sub>2</sub>O) proposed by [Laurent et al. \(2014\)](#) suggests the partial melting of a crustal source of sedimentary origin (S-type) (**Fig. 5e**).

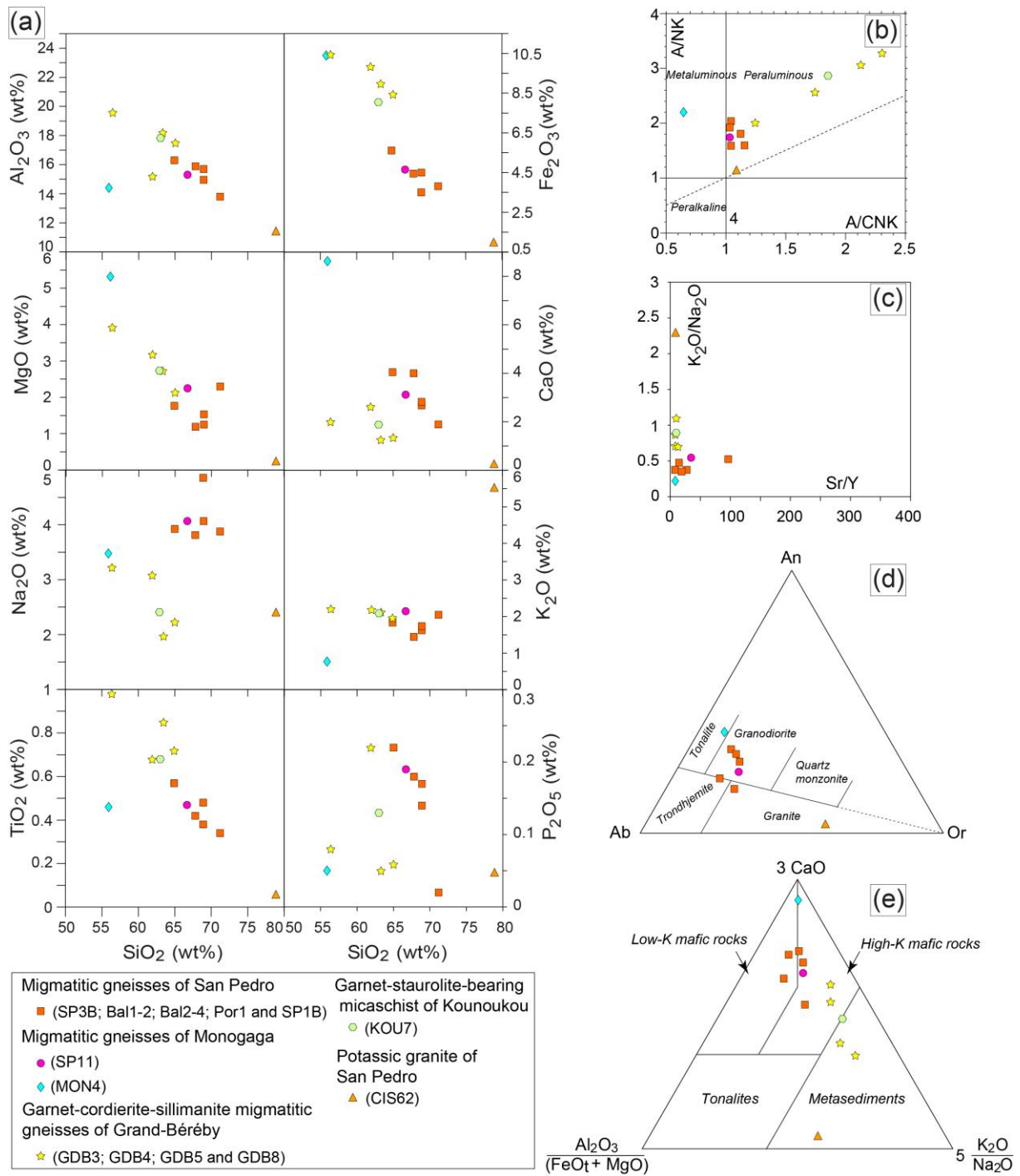


**Fig. 5.** Major element geochemistry of the studied rocks in Harker diagrams (a), in an A/NK vs. A/CNK diagram (b), K<sub>2</sub>O/Na<sub>2</sub>O vs. Sr/Y diagram (c). Normative An–Ab–Or triangle (O'Connor, 1965) showing the migmatitic gneiss composition of San Pedro and Monogaga (d) and (e) ternary diagram Al<sub>2</sub>O<sub>3</sub>/(FeO<sub>T</sub> + MgO); 3 \* CaO; 5 \* (K<sub>2</sub>O/Na<sub>2</sub>O) of Laurent et al. (2014) on which the composition of the migmatitic gneisses of San Pedro and Monogaga is plotted.

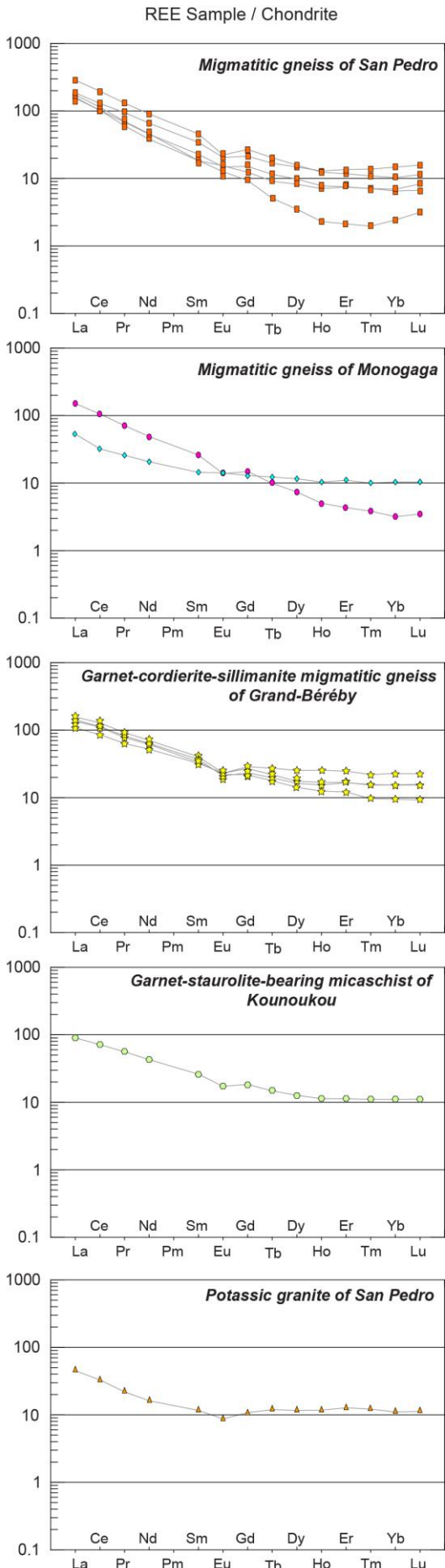
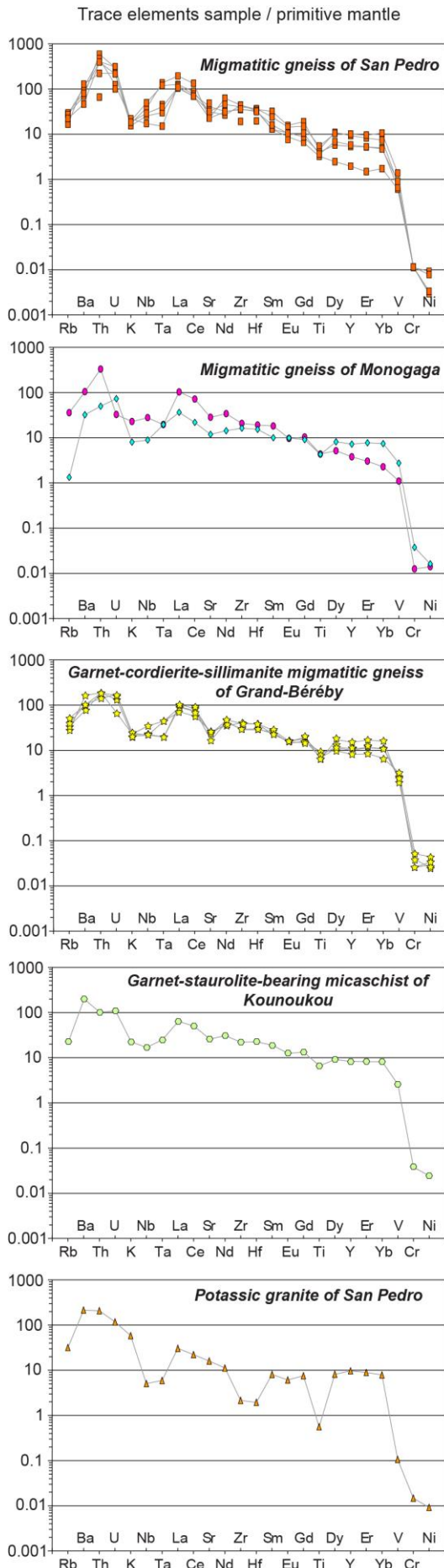


**Fig. 6.** Primitive mantle-normalized trace element (McDonough et al., 1992) and chondrite normalized REE (Sun and McDonough, 1989) spidergrams of the studied rocks. For legend, see Fig. 4.

### 5.3. Zircon U-Pb geochronology and Hf isotopes

#### *- Migmatitic gneiss of San Pedro*

The zircon grains obtained from sample SP3B display variable sizes (50 to 300  $\mu\text{m}$ ) (**Fig. 7a**). In cathodoluminescence (CL) images, the zircon grains show quite heterogeneous internal textures and morphologies. Most grains are euhedral with rounded facets showing magmatic oscillatory zoning, locally overgrown by dark rims. For some of these grains, the oscillatory zoning is blurred by diffuse zones attributed to dissolution-precipitation. Sixty-eight analyses were performed on fifty-three zircons. One other analysis was rejected as containing a very high U concentration >1500 ppm. Thirty-one concordant analyses returned ages ranging from ca. 3241 Ma to ca. 2827 Ma (**Fig. 8a, 8b**). On the probability density plot, the data may be grouped into two main populations including: 1) age cluster from ca. 3241 Ma to ca. 3128 Ma ( $n = 22$ ) with Th/U between 2.45 and 0.09 but without statistically defined peaks, 2) age cluster from ca. 3113 Ma to ca. 3078 Ma ( $n = 3$ ), and three isolated analyses returning dates at  $2993 \pm 32$  Ma (Th/U = 0.28),  $2975 \pm 4$  Ma (Th/U = 0.23) and  $2827 \pm 5$  Ma (Th/U = 0.14).

Twenty-three Lu-Hf analyses were performed on concordant zircons of SP3B. The zircons have variable  $^{176}\text{Lu}/^{177}\text{Hf}$  ratios (0.00077–0.00790) and  $^{176}\text{Hf}/^{177}\text{Hf}$  ratios (0.280428–0.280702) corresponding to subchondritic  $\epsilon_{\text{Hf}}$  between -9.4 and -0.3. On the plot showing apparent ages obtained for individual zircon vs initial  $^{176}\text{Hf}/^{177}\text{Hf}$  composition (**Fig. 9a**) the data distribution over 9  $\epsilon_{\text{Hf}}$  units is particularly marked for the age cluster from ca. 3241 Ma to ca. 3128 Ma and exceeds the accuracy of the analytical technique for this dataset ( $\sim 3$   $\epsilon_{\text{Hf}}$  units). All other age clusters exhibit a constant and restricted  $^{176}\text{Hf}/^{177}\text{Hf}$  ratio between 0.280560 and 0.280680 ( $\sim 3$   $\epsilon_{\text{Hf}}$  units), which may be considered as constant considering analytical technique's accuracy.

#### *- Migmatitic gneiss of Monogaga*

The zircons from sample SP11 are of variable sizes (50 to 300  $\mu\text{m}$ ) (**Fig. 7b**). The scanning electron microscope (SEM) images of all zircons in sample SP11 show euhedral grains with oscillatory zoning, with few grains showing rounded facets. Some zircon grains show homogeneous overgrowth zones. A few zircon crystals devoid of internal growth zoning, have grown aside a pre-existing core. One hundred and forty-one analyses were performed on one hundred zircons. One hundred and thirty concordant analyses returned ages ranging from ca.

3263 Ma to 2071 Ma (**Fig. 8d, 8e**). On the data distribution plot, several age populations are distinguished : 1) an age cluster from ca. 3263 Ma to 3234 Ma (n = 18) with Th/U comprised between 0.43 and 0.27 and giving a weighted mean age of  $3245 \pm 4$  Ma (MSWD = 1.6); 2) a nearly continuous record from ca. 3226 Ma to 3124 Ma (n = 64) with a potential peak around ca. 3200 Ma and Th/U values between 0.52 and 0.20; 3) an age cluster from ca. 3108 Ma to 3076 Ma (n = 10) with Th/U ratio ranging between 0.49 and 0.20; 4) a sub-continuous record of ages from ca. 3057 Ma to 2984 Ma (n = 11) with Th/U comprised between 0.41 and 0.18 showing a distinct peak at about ca. 3020 Ma; 5) an age cluster from ca. 2965 Ma to 2823 Ma (n = 13) showing a distinct peak at about 2832 Ma; 6) a sub-continuous record of ages from ca. 2787 Ma to 2695 Ma (n = 9) and Th/U comprised between 0.18 and 0.01; and 7) an age cluster from ca. 2082 Ma to 2071 Ma (n = 4) and Th/U comprised between 0.21 and 0.06 and giving a weighted mean age of  $2076 \pm 7$  Ma (MSWD = 0.45). The zircon cores belonging to the oldest age cluster from ca. 3241 and 3078 Ma returned Th/U between 0.43 and 0.27.

Sixteen analysis points were performed to analyse the Lu-Hf isotope composition on concordant zircons of SP11. The zircons of SP11 have variable  $^{176}\text{Lu}/^{177}\text{Hf}$  ratios of 0.00057–0.00104 with, however, relatively homogeneous  $^{176}\text{Hf}/^{177}\text{Hf}$  ratios of 0.280696–0.280829 corresponding to superchondritic  $\epsilon_{\text{Hf}}$  between -4.1 and +1.9. On the plot showing apparent ages obtained for individual zircon vs initial  $^{176}\text{Hf}/^{177}\text{Hf}$  composition (**Fig. 9a**), zircon cores dated between ca. 3241 and 3078 Ma present initial  $^{176}\text{Hf}/^{177}\text{Hf}$  that spread over two  $\epsilon_{\text{Hf}}$  units, remaining within the precision of the analytical technique. Taken conjointly, these results show a nearly constant initial  $^{176}\text{Hf}/^{177}\text{Hf}$  composition over ca. 200 Myrs (**Fig. 9c**). One analysis of a zircon dated at  $2957 \pm 11$  Ma return initial  $^{176}\text{Hf}/^{177}\text{Hf}$  of 0.280829 and  $\epsilon_{\text{Hf}} = -2.2$ . This analysis departs from the near constant array preserved in older grains and argues for late crustal reworking.

The zircons obtained from sample MON4 display variable sizes (50 to 300  $\mu\text{m}$ ) (**Fig. 7c**). The SEM images of all the zircons in the MON4 sample show oscillatory zoning and a high proportion of rounded shapes. Most of the grains are affected by fracturing due to sample processing or radiation damage of the crystal lattice. Forty-eight analyses were performed on forty zircons. Two analyses were filtered away (discordance, high U content,  $U > 1500$  ppm). The remaining thirty-five analyses yield ages ranging from ca. 3328 Ma to 2815 Ma (**Fig. 8g, 8h**). On the distribution plot, the data may be grouped into two main populations including age spans: 1) a cluster from ca. 3328 Ma to 3156 Ma (n = 22 with Th/U comprised between 0.82 and 0.01 with a clear peak at ca. 3260 Ma but not returning a statistically robust population; 2)

a sub-continuous record of ages from ca. 3129 Ma to 2869 Ma (n = 13) with Th/U comprised between 0.05 and 0.00 showing no distinct peak.

Seven Lu-Hf analyses were performed on concordant zircons of MON4. These grains have variable  $^{176}\text{Lu}/^{177}\text{Hf}$  ratios of 0.00104–0.00197 with initial  $^{176}\text{Hf}/^{177}\text{Hf}$  ratios of 0.28071–0.28077 corresponding to superchondritic  $\epsilon_{\text{Hf}}$  between +0.7 and +3.8 (**Fig. 9a**). Note that these analyses were solely obtained on zircon cores presenting apparent age comprised between ca. 3230 Ma and 3310 Ma. The initial  $^{176}\text{Hf}/^{177}\text{Hf}$  ratios remain constant over the period considered and therefore suggest that the sample was affected by a lead loss (**Fig 9d**) or a protracted period of zircon dissolution/precipitation and/or crystallization.

*- Garnet-cordierite-sillimanite migmatitic gneiss of Grand-Béréby*

The zircons obtained from sample GDB8 display variable sizes (50 to 200  $\mu\text{m}$ ) (**Fig. 7d**). The CL images of all the zircons in the GDB8 show oscillatory to complex zoning with rare euhedral shapes. Many grains are rounded. Ninety-three analyses were performed on eighty-seven zircons (**Fig. 8j, 8k**). Seventy-eight concordant analyses returned ages ranging from ca. 2670 Ma to 2060 Ma. On the KDE (Kernel Density Estimation) plot, the data may be grouped as follows: 1) a single age at  $2670 \pm 11$  Ma; 2) two single ages at ca. 2480 Ma and 2472 Ma; 3) three analyses yielded ages between ca. 2213 Ma and 2193 Ma; 4) a sub-continuous record of ages from ca. 2182 Ma to 2086 Ma (n = 62) and Th/U comprised between 5.15 and 0.01 showing several peaks at ca. 2175 Ma, 2145 Ma, 2130 Ma, 2115 Ma and 2090 Ma; 5) age cluster from ca. 2077 Ma to 2060 Ma (n = 9) with Th/U values between 0.54 and 0.09 and giving a weighted mean age of  $2069 \pm 4$  Ma (MSWD = 4.2). The high uncertainties in the  $^{238}\text{U}/^{206}\text{Pb}$  data might be due to a disturbance in the U-Pb system.

Ten analyses were performed by the Lu-Hf method on concordant zircons of GDB8. The zircons of GDB8 have variable  $^{176}\text{Lu}/^{177}\text{Hf}$  ratios of 0.00010–0.00133 with initial  $^{176}\text{Hf}/^{177}\text{Hf}$  ratios of 0.28141–0.28155, corresponding to superchondritic  $\epsilon_{\text{Hf}}$  between 0.0 and +5.5 (**Fig. 9e**). The spread in initial  $^{176}\text{Hf}/^{177}\text{Hf}$  analyses is compatible with a detrital sedimentary origin pointing to several sources (**Fig. 9f**).

*-Garnet-staurolite-bearing micaschist of Kounoukou*

The zircons obtained from sample KOU7 display variable sizes (50 to 250  $\mu\text{m}$ ) (**Fig. 7e**). The CL images of all zircons in the KOU7 sample show euhedral elongated shapes with oscillatory magmatic zoning. Few grains display rounded facets. One hundred and nineteen analyses were performed on one hundred and ten zircons (**Fig. 8m**). Ninety-two concordant analyses returned

ages ranging from ca. 2214 Ma to 2081 Ma. On the probability density plot, the data may be grouped as follow: 1) two single ages at ca. 2214 Ma and 2201 Ma; 2) one age cluster from ca. 2187 Ma to 2184 Ma ( $n = 3$ ) with obtained Th/U values between 0.86 and 0.62 and giving a weighted mean age of  $2186 \pm 3$  Ma (MSWD = 0.53); 3) two single ages at ca. 2165 Ma and 2157 Ma; 4) one age cluster from ca. 2140 Ma to 2131 Ma ( $n = 7$ ) with Th/U comprised between 1.13 and 0.34 and giving a weighted mean age of  $2136 \pm 3$  Ma (MSWD = 1.07); 5) a sub-continuous record of ages from ca. 2123 Ma to 2090 Ma ( $n = 77$ ) with Th/U comprised between 2.49 and 0.24 showing a peak at ca. 2109 Ma; 6) a single zircon dated at  $2082 \pm 4$  Ma with Th/U = 0.50.

Twenty-three Lu-Hf analyses were performed on concordant zircons of KOU7. The zircons of KOU7 have variable  $^{176}\text{Lu}/^{177}\text{Hf}$  ratios of 0.00067–0.00142 with initial  $^{176}\text{Hf}/^{177}\text{Hf}$  ratios ranging from 0.281477 and 0.281525, and corresponding to superchondritic  $\epsilon_{\text{Hf}}$  between +1.5 and +4.9 (**Fig. 9e and 9g**).

*- Potassic granite*

Sample CIS62 exhibits zircons that vary in sizes (50 to 200  $\mu\text{m}$ ) with generally prismatic shapes (**Fig. 7f**). The CL images show oscillatory magmatic zoning. Sixty-three analyses were obtained from this sample, of which fifty-three are discordant or rich in U ( $\text{U} > 1500$  ppm). Nine concordant to near concordant analyses spread in ages from ca. 2312 Ma to ca. 2084 Ma (**Fig. 8p, 8q**). These analyses can be grouped as follow: 1) one single analysis dated at  $2312 \pm 51$  Ma with Th/U = 0.99; 2) one single analysis dated at  $2205 \pm 42$  Ma with Th/U = 0.02; 3) one single analysis dated at  $2126 \pm 12$  Ma with Th/U = 0.09; 4) a population ranging from ca. 2105 Ma to 2096 Ma ( $n = 5$ ) with Th/U comprised between 2.49 and 0.24 returning a weighted mean age of  $2100 \pm 5$  Ma (MSWD = 1.7); 5) one single analysis dated at  $2084 \pm 6$  Ma with Th/U = 0.44. The date of  $2084 \pm 6$  Ma is tentatively interpreted as the crystallisation age for the potassic granite. The high uncertainties in the  $^{238}\text{U}/^{206}\text{Pb}$  data might be due to a disturbance in the U-Pb system.

Eleven analyses were performed by the Lu-Hf method on concordant zircons of CIS62. Analyses of CIS62 have variable  $^{176}\text{Lu}/^{177}\text{Hf}$  ratios of 0.00029–0.00297 with initial  $^{176}\text{Hf}/^{177}\text{Hf}$  ratios ranging from 0.28120 to 0.28151 corresponding to  $\epsilon_{\text{Hf}}$  values between -8.5 and +6.5 (**Fig. 9e**). The spread of initial  $^{176}\text{Hf}/^{177}\text{Hf}$  with regards to the U/Pb analyses is compatible with two contrasted sources (**Fig. 9h**).

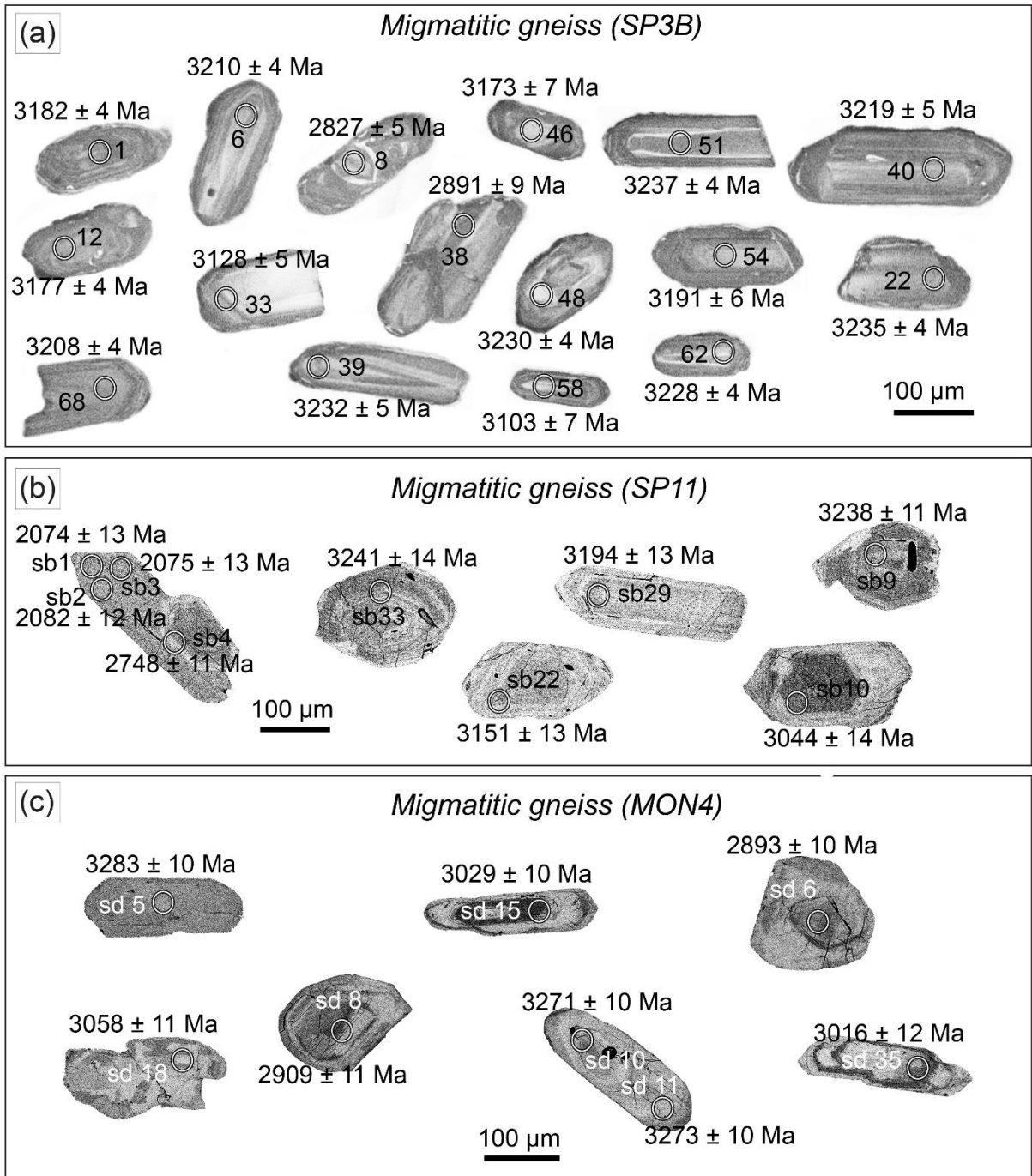


**Fig. 7.** Cathodoluminescence (CL) images of representative zircons grains from the studied rocks. Circles indicate the location of U-Pb analyses.

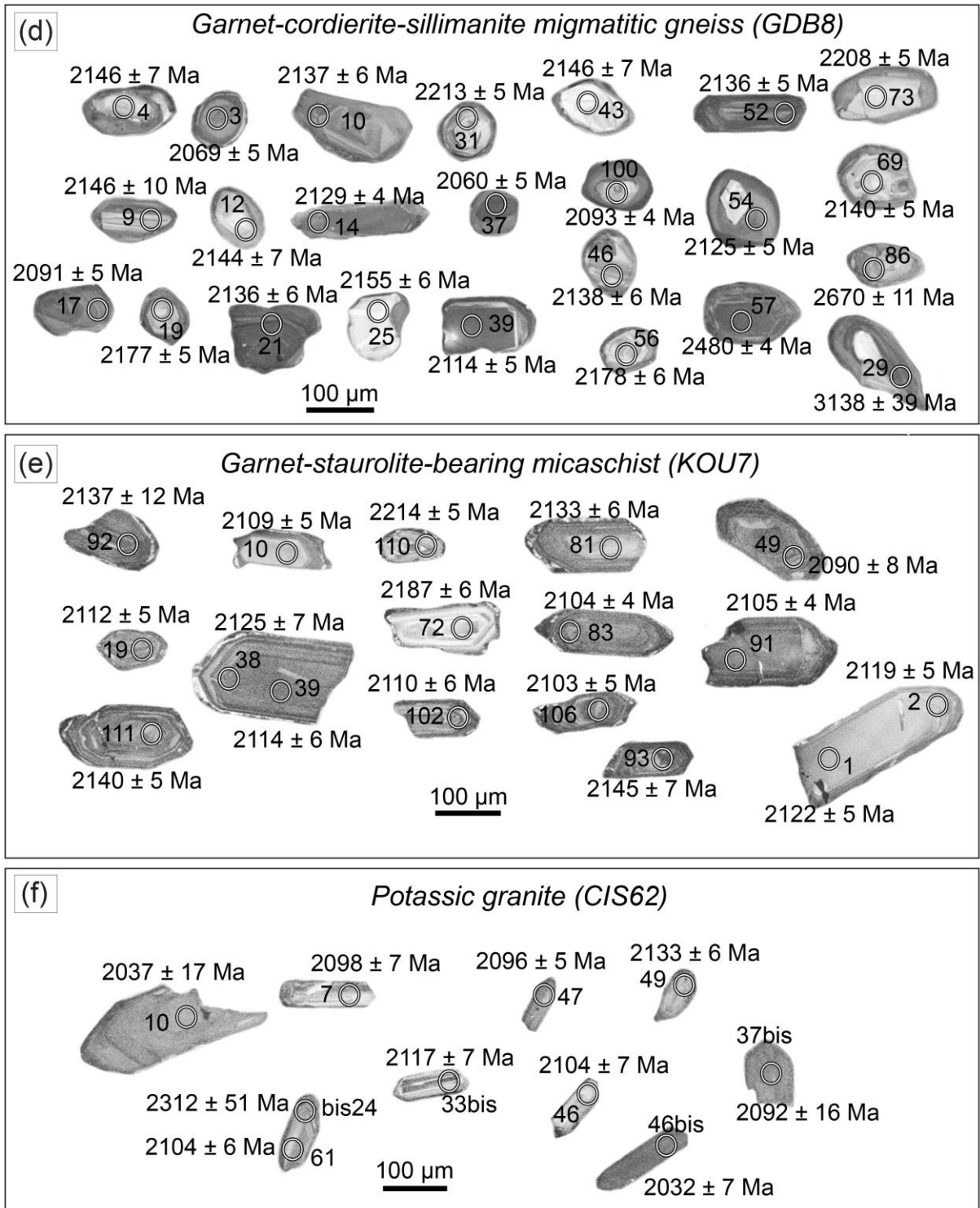
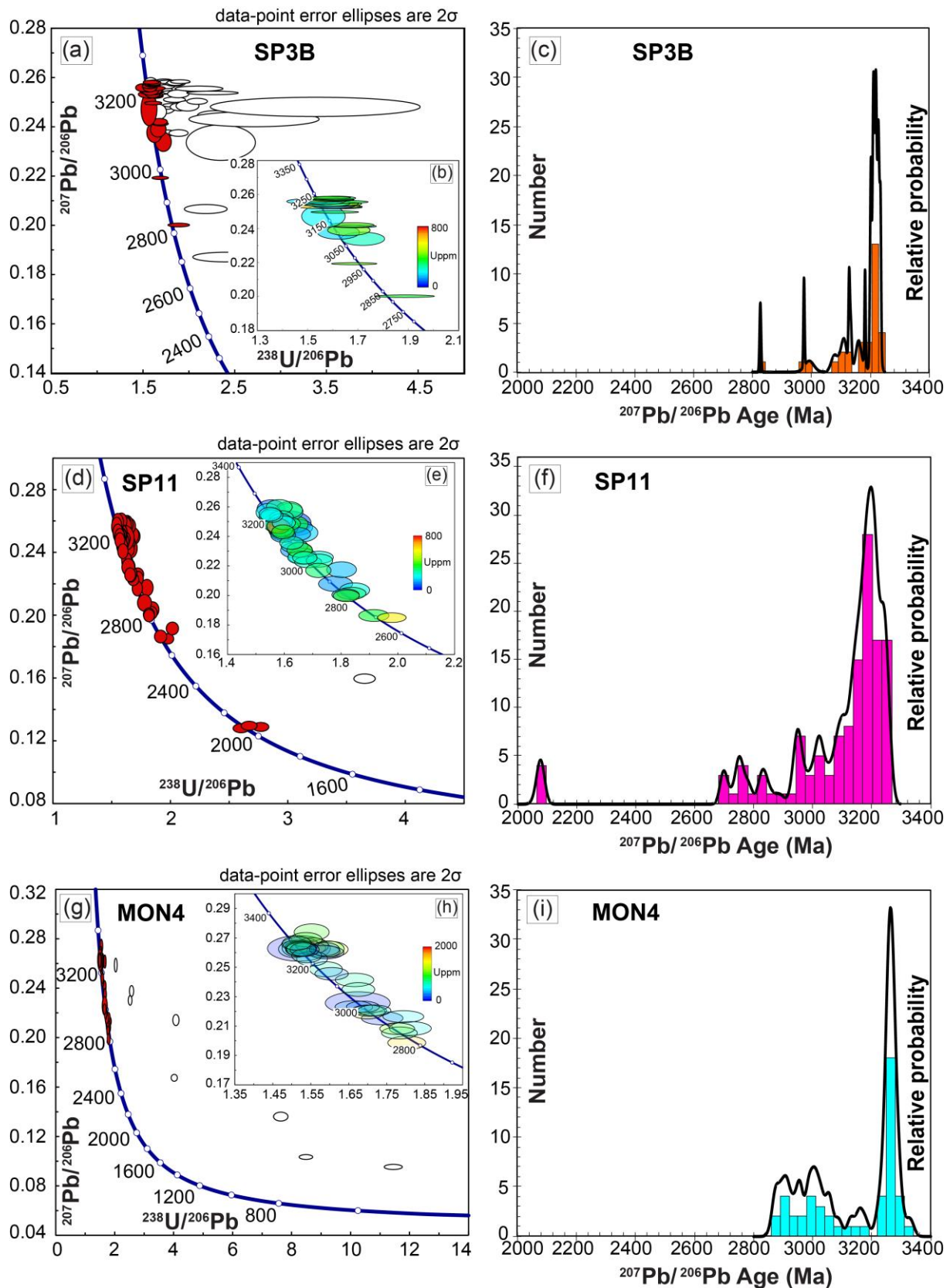


Fig. 7. (continued).



**Fig. 8.** U/Pb concordia diagrams (left) and distribution plots (right) for zircon of all samples dated using LA-ICPMS. For each sample, in the main concordia diagram, the analyses filled in red have a concordance between -2% and +5%, and the white filled analyses are discordant and not selected for interpretation. In the inset diagram, the concordant to near-concordant analyses are color coded following U concentration. (a, b, c) Sample SP3B, migmatitic gneiss from San

Pedro. (d, e, f). Sample SP11, migmatitic gneiss from Monogaga. (g, h, i) Sample MON4, migmatitic gneiss from Monogaga. Note that for both clusters of data, the U concentration increases towards younger ages. (j, k, l). Sample GDB8, garnet cordierite-sillimanite migmatitic gneiss of Grand-Béréby. (m, n, o) Sample KOU7, garnet-staurolite-bearing micaschist of Kounoukou. (p, q, r) Sample CIS62, potassic granite.

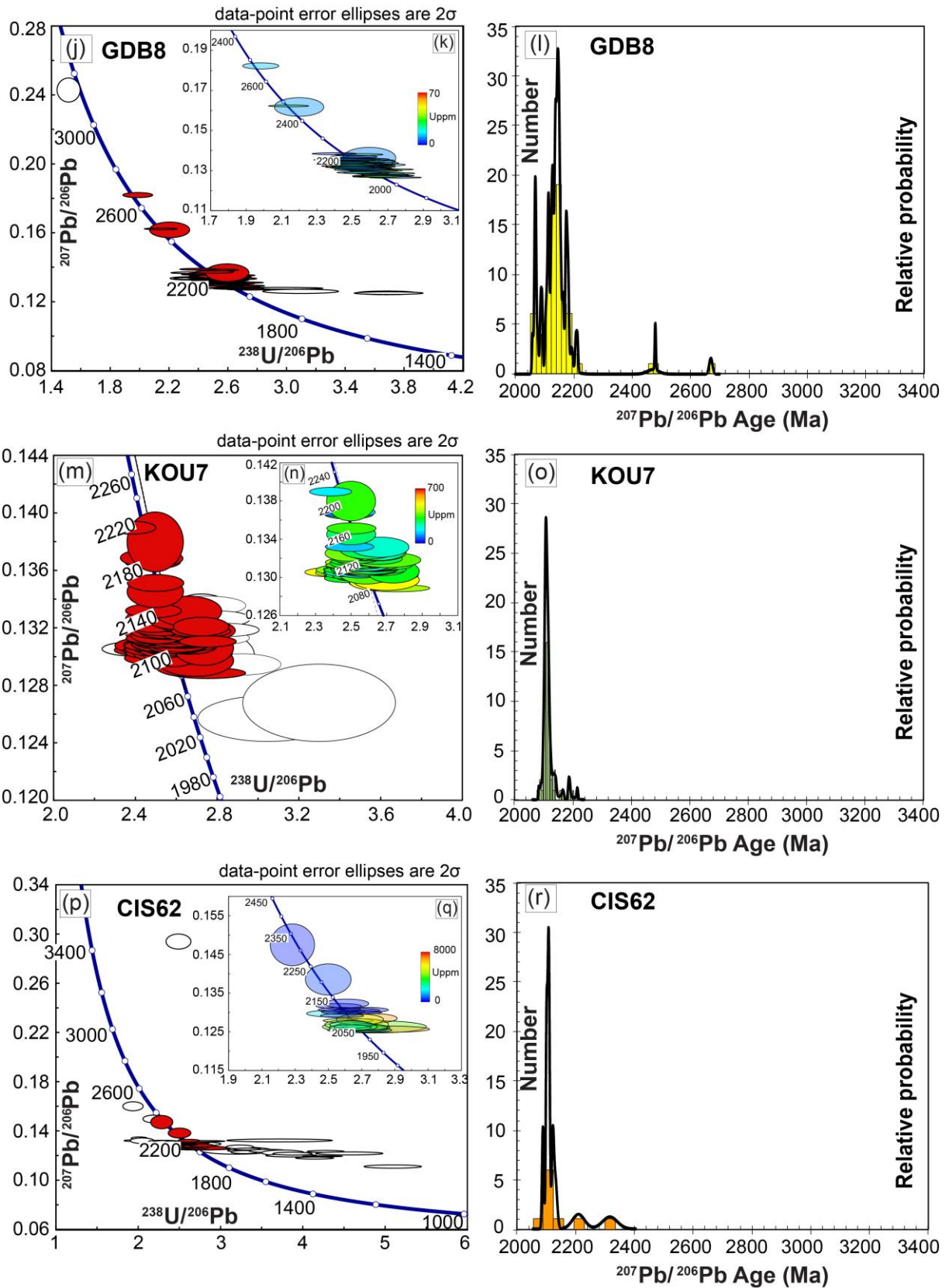
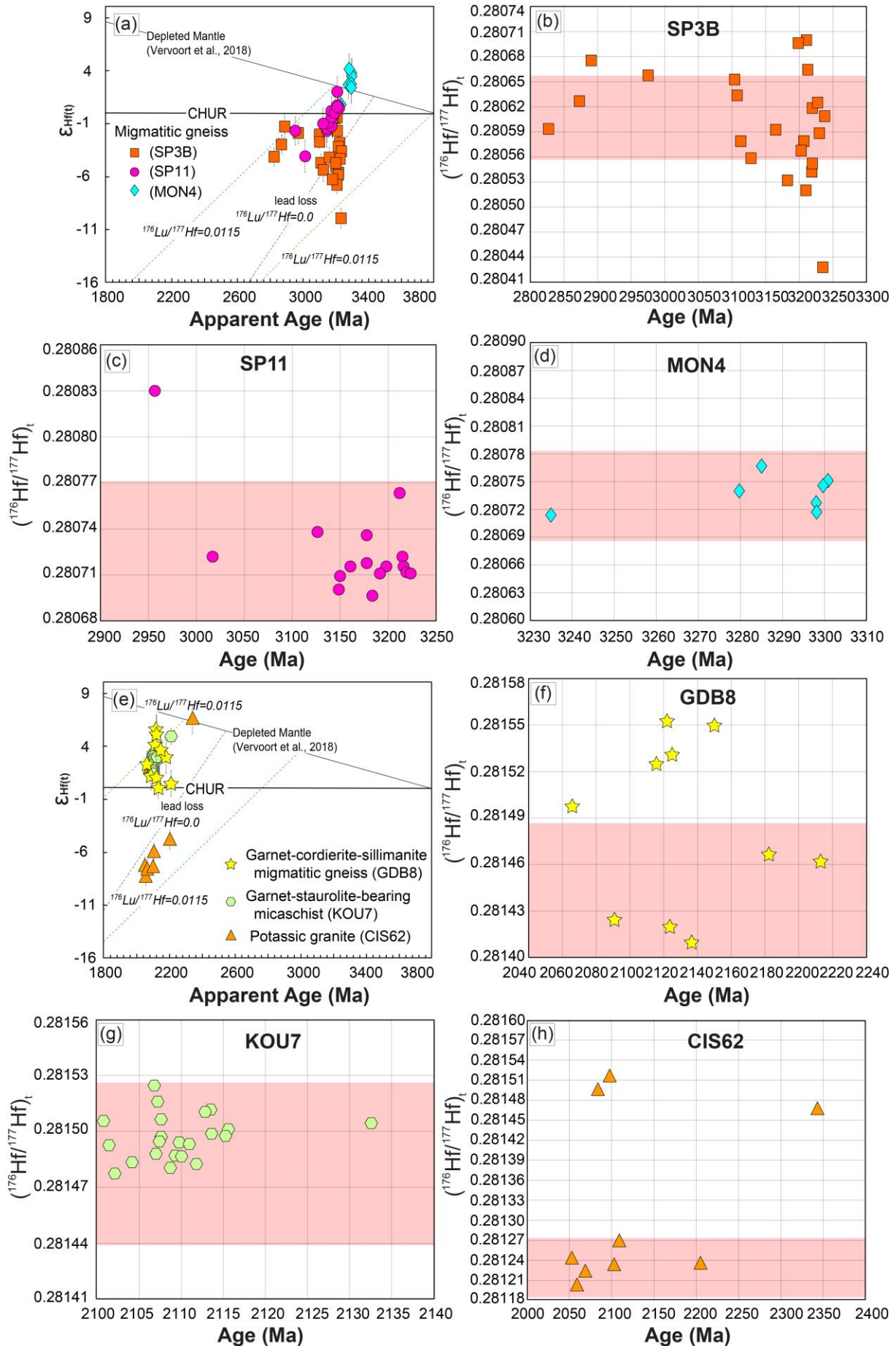


Fig. 8. (continued).



**Fig. 9.** Compilation of zircon U-Pb and Lu-Hf data obtained in the course of this study. (a and e):  $\epsilon_{\text{Hf}(t)}$  vs. apparent  $^{207}\text{Pb}/^{206}\text{Pb}$  age diagrams for individual spots for migmatitic gneiss of San Pedro SP3B and Monogaga SP11, MON4 (a), garnet-cordierite-sillimanite migmatitic gneiss of Grand-Béréby GDB8, garnet-staurolite-bearing micaschist of Kounoukou KOU7 and potassic granite CIS62 (e). (b, c, d, f, g and h):  $^{176}\text{Hf}/^{177}\text{Hf}_t$  vs. apparent  $^{207}\text{Pb}/^{206}\text{Pb}$  age diagrams for individual spots of zircon from the migmatitic gneiss of San Pedro SP3B (b), Monogaga SP11 (c), MON4 (d), garnet-cordierite-sillimanite migmatitic gneiss of Grand-Béréby GDB8 (f), garnet-staurolite-bearing micaschist of Kounoukou KOU7 (g) and potassic granite CIS62 (h). Crustal evolution trends are calculated with a value of  $^{176}\text{Lu}/^{177}\text{Hf} = 0.0115$ , value for average present-day continental crust. CHUR = chondritic uniform reservoir; DM = depleted mantle after [Vervoort et al. \(2018\)](#). Red square indicating the external reproducibility (accuracy) of the instrument, data plowshowing near constant  $^{176}\text{Hf}/^{177}\text{Hf}_t$ .

## 6. DISCUSSION

### 6.1. Origin of the metamorphic rocks

Deciphering the nature of the protolith of high-grade gneisses is not always an easy task, especially in case of partial melting.

The mineral assemblage associated with the garnet-staurolite-bearing micaschist of Kounoukou (KOU7) and of the garnet sillimanite migmatitic gneiss from Grand-Béréby (GDB8) points towards a sedimentary (pelitic) origin. Both metapelites display high mean content in  $\text{Al}_2\text{O}_3$  (> 15 wt%) and  $\text{Fe}_2\text{O}_3$  (> 7 wt%) together with moderate concentration of  $\text{MgO}$  (> 2 wt%) and low  $\text{CaO}$  (< 2 wt%). Such compositions are compatible with those of metapelitic rocks ([Bucher and Grapes, 2011](#)).

The potassic granite CIS62 has pronounced negative Nb, Ta, Zr, Hf and Ti anomalies, weak negative Eu anomaly and very low contents in  $\text{Al}_2\text{O}_3$ ,  $\text{Fe}_2\text{O}_3$ ,  $\text{MgO}$  and  $\text{CaO}$  compared to all other rocks (**Figs. 5 and 6**). Its high K content suggests a S-type granite, as shown in the ternary diagram  $\text{Al}_2\text{O}_3/(\text{FeO}_t + \text{MgO})$ ;  $3 * \text{CaO}$ ;  $5 * (\text{K}_2\text{O}/\text{Na}_2\text{O})$  proposed by [Laurent et al. \(2014\)](#)

The migmatitic gneisses of San Pedro and the migmatitic gneiss of Monogaga SP11 cluster in a relatively homogeneous group in compositional and classification diagrams (**Fig. 5**), while the MON4 gneiss of Monogaga is very different from this group in most of the major element diagrams. Overall, the major element geochemical compositions of migmatitic gneisses are different from those of the metasediments and the potassic granite. On the other hand, the trace and REE patterns are relatively similar for the gneisses and metasediments. The migmatitic gneisses exhibit geochemical compositions of Archean TTGs ( $\text{SiO}_2 > 64$  wt%,  $A/\text{CNK} \sim 1$ ) as

defined by [Moyen and Martin \(2012\)](#). They are enriched in Light Rare-Earth Elements (LREE) with positive Eu anomalies ( $\text{Eu}/\text{Eu}^* = 0.64\text{--}1.05$ ) and display high Sr/Y ratios. The predominance of quartz and feldspar accounts for the bulk  $\text{SiO}_2$ ,  $\text{Al}_2\text{O}_3$ ,  $\text{Na}_2\text{O}$  and  $\text{K}_2\text{O}$  contents of these rocks, and is consistent with a granodioritic bulk composition. Based on the geochemical data and the character of the U-Pb analyses discussed in detail in Section 6.2, which show two major events (the protolith emplacement at ca. 3250-3200 Ma and ca. 2950-2800 Ma reworking leading to crystallization of the younger zircon population, **Fig. 9**), we suggest a magmatic protolith of the migmatitic gneisses of San Pedro and Monogaga.

## 6.2. Archean geochronological record of the Sassandra-Cavally domain

The migmatitic gneiss samples from San Pedro (SP3B) and Monogaga (MON4 and SP11) returned a complex age distribution spreading from the the Archean (SP3B, MON4 and SP11) to the Paleoproterozoic eras (SP11) (**Fig. 10**). U-Pb analyses acquired on MON4 and SP11 exhibit several concordant date clusters with initial  $^{176}\text{Hf}/^{177}\text{Hf}$  ratios that are constant for zircon dates ranging from ca. 3250 Ma and 3000 Ma. The nearly invariant initial  $^{176}\text{Hf}/^{177}\text{Hf}$  ratio observed for both samples is characteristic for zircons that have undergone ancient lead-loss ([Fisher et al., 2014](#)). Alternatively, this spread of ages may be contributed to a prolonged period of dissolution/precipitation and/or crystallisation in the presence of melt but in a closed system ([Guergouz et al., 2018](#); [Vanderhaeghe et al., 2019](#)). Many of the ages spreading from ca. 3250 Ma and 3000 Ma were obtained on cores of texturally equilibrated zircons with oscillatory zoning. In order to further test the hypothesis of dissolution/precipitation mechanism, systematic core/rim analyses need to be acquired as well as zircon trace element analyses. It was not done in this study and will be better implemented in our futures studies of the rocks from the Archean – Paleoproterozoic boundary terranes. In any case, these features suggest that the protolith of these rocks corresponds to material extracted from the mantle at ca. 3200 Ma. The age clusters derived from U-Pb analyses in the sample SP3B together with the Hf composition suggest that the younger groups ranging in age from ca. 3113 Ma to 2827 Ma, preserving constant initial  $^{176}\text{Hf}/^{177}\text{Hf}$  composition were affected by ancient lead loss or a prolonged period of zircon dissolution/precipitation and/or crystallization. In contrast the age cluster from ca. 3241 Ma to ca. 3128 Ma appears to reflect the mixing of several zircon populations associated with contrasted initial  $^{176}\text{Hf}/^{177}\text{Hf}$  composition (**Fig. 9b**). This may point towards the contribution of diverse zircon sources in the original protholith (magmatic zircons combined with one or more inherited zircon populations). The sparse Hf analyses of zircon that returned apparent zircon ages comprised between ca. 2800 Ma and 3000 Ma either exhibit near

constant initial  $^{176}\text{Hf}/^{177}\text{Hf}$  (SP3B) or show higher  $^{176}\text{Hf}/^{177}\text{Hf}$  ratio (SP11). Whereas the former may also be interpreted as an ancient lead loss event, the latter points towards a zircon producing event ca. 2950 Ma.

For sample SP11 the weighted mean  $^{207}\text{Pb}/^{206}\text{Pb}$  age of  $3245 \pm 4$  Ma acquired on the older age cluster is interpreted as the age of the protolith. The analysis showing an apparent age at  $2957 \pm 11$  Ma returned an initial  $^{176}\text{Hf}/^{177}\text{Hf}$  ratio of 0.280829 that contrasts with the near constant initial  $^{176}\text{Hf}/^{177}\text{Hf}$  ratio obtained on the ca. 3241 and 3078 Ma data cluster (**Fig. 9c**). The initial  $^{176}\text{Hf}/^{177}\text{Hf}$  ratio of 0.280829 is compatible with a zircon producing event at ca. 2950 Ma. Consequently, the protolith age for SP11 migmatitic gneiss is interpreted to have formed at  $3245 \pm 4$  Ma further affected by a melt crystallization event at ca. 2950 Ma (one analysis returned a concordant age at  $2957 \pm 11$  Ma. The latter event remains poorly constrained as based on a single analysis yet may be indicative of a Mesoproterozoic migmatitization stage that could have been the driver of the lead loss recorded. More analyses should be conducted on the youngest age population in the sample to further constrain the age of this magmatic event.

For MON4 and SP3B, the spread of ages resulting from ancient lead loss makes it impossible to calculate a statistically robust magmatic age for the protolith. Accordingly, the older  $^{206}\text{Pb}/^{207}\text{Pb}$  apparent ages are tentatively proposed as the age of the protolith for both MON4 and SP3B samples and are  $3328 \pm 13$  Ma and  $3238 \pm 4$  Ma, respectively. Note that the complex Hf record for sample SP3B may reflect the presence of inherited xenocrysts in the protolith source which further raise uncertainty for its age attribution.

In the absence of  $^{176}\text{Hf}/^{177}\text{Hf}$  analysis in MON4 for the younger age cluster it remains difficult to evaluate the nature of the younger age cluster. Yet by analogy with sample SP11, it is proposed that the age of the protolith of ca. 3260 Ma was affected by a melt crystallization event at  $2869 \pm 13$  Ma provided by the apparent age of the youngest zircon.

The ages obtained appear slightly older than those obtained by Pb-Pb evaporation at  $3207 \pm 7$  Ma acquired on restricted number of zircons collected from the San Pedro gneisses ([Kouamelan et al., 1997b, 2015; Kouamelan, 1996](#)). The age discrepancy between the youngest age group may be related to the restricted number of grains analysed using Pb-Pb evaporation.

All the zircons belonging to younger age clusters including the four analyses that were obtained from zircons rims were associated with overall low Th/U ratios  $< 0.50$ . Magmatic zircons present Th/U  $> 0.50$  ([Skublov et al., 2009; Pystin and Pystina, 2015; Rubatto, 2002](#)), while metamorphic zircons have Th/U comprised between 0.10 and 0.30 ([Pystin and Pystina, 2015](#)), or even  $< 0.10$  ([Rubatto, 2002](#)). The age of  $2076 \pm 7$  Ma has been obtained on a large euhedral overgrowth crystallized around an inherited zircon core with an age of  $2748 \pm 11$  Ma (**Fig. 7b**)

and is likely to represent the age of high-grade metamorphism, possibly in the presence of a silicate melt.

Such Paleoproterozoic overprint is likely to have disturbed further the ancient age record related to the lead loss at ca. 2700 recorded in the same sample (**Fig. 8**). Accordingly, it is proposed that the San Pedro and Monogaga units represent Paleoproterozoic protoliths reworked through deformation and metamorphism (including partial melting linked to the migmatitization) in the Mesoarchean and the Paleoproterozoic.

The age spread recorded in the samples from both localities is similar to that recorded in Sierra Leone, Liberia, and Guinea (Barth et al., 2002; De Waele et al., 2015; Kouamelan et al., 1997b; Thiéblemont et al., 2004) but also in the Reguibat Shield (Lahondère et al., 2003; Potrel et al., 1998). Across the Sassandra shear zone, Archean rocks were historically ascribed to two main periods of crust formation between ca. 3260–3050 Ma and ca. 2960–2850 Ma (Barth et al., 2002; De Waele et al., 2015; Kouamelan et al., 1997b; Rollinson, 2016; Thiéblemont et al., 2004). The results obtained here further document this two-staged period with initial crust extrusion at about ca. 3300–3250 Ma followed by a major lead loss event at ca. 2960–2850 Ma. The nature of the magmatic and metamorphic processes underlying the generation of these two broad populations remains largely unknown.

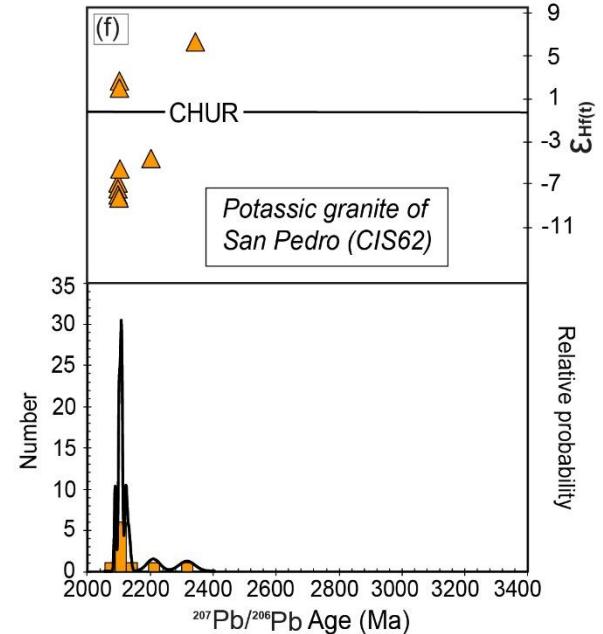
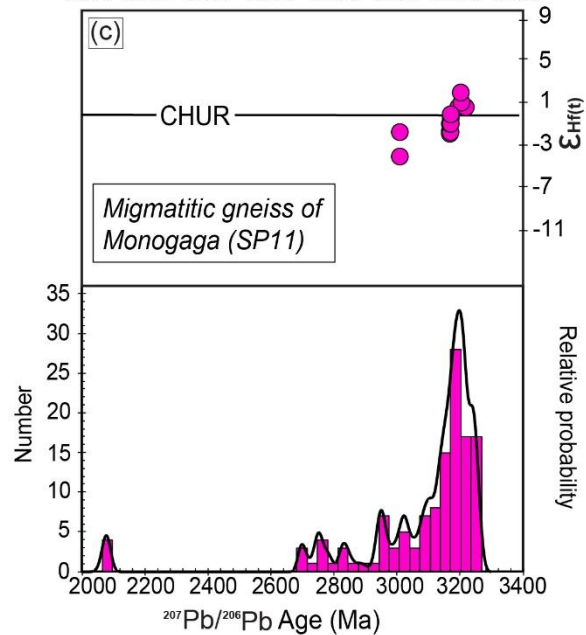
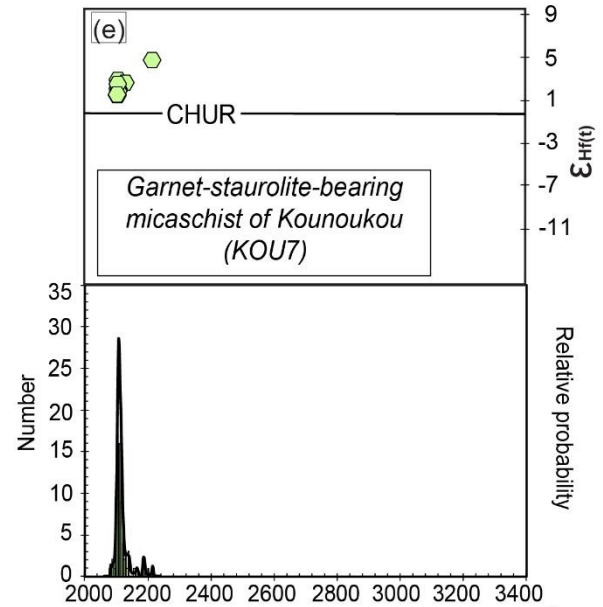
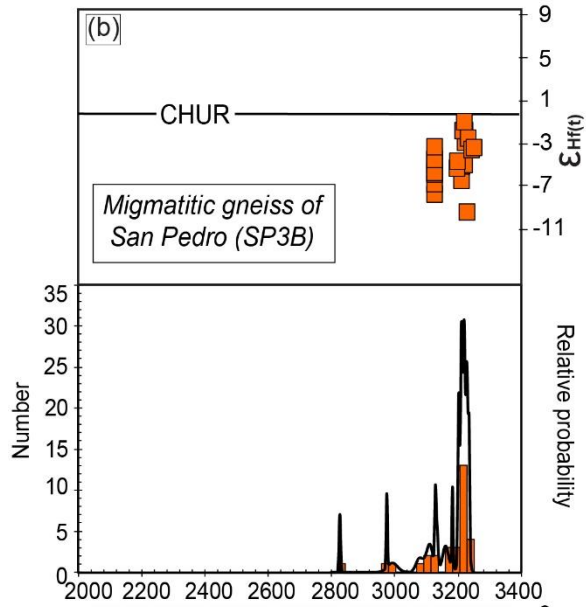
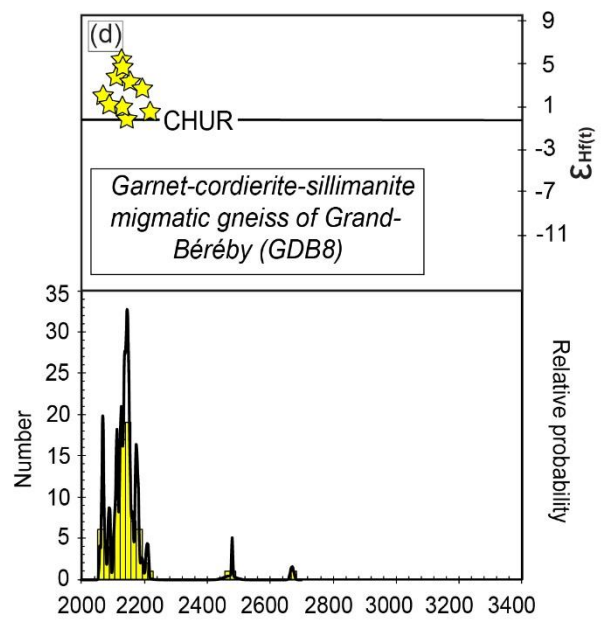
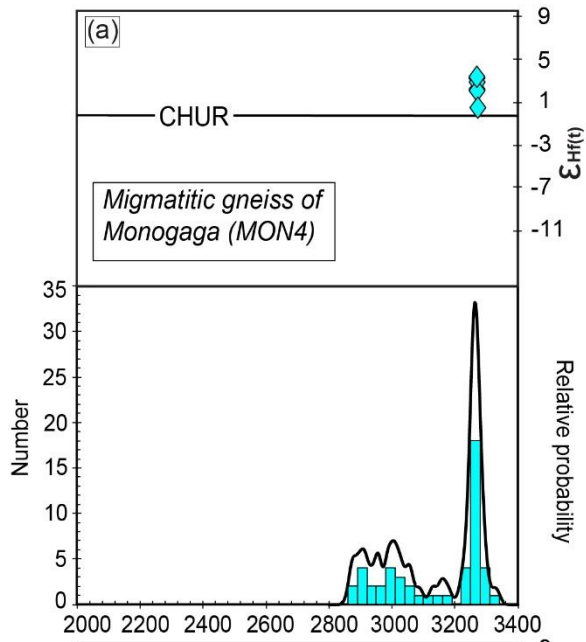


**Fig. 10.**  $\epsilon_{\text{Hf}(t)}$  and probability density plots for all U-Pb zircon data acquired on the samples. (a) migmatitic gneiss of Monogaga MON4; (b) migmatitic gneiss of San Pedro SP3B; (c) migmatitic gneiss of Monogaga SP11; (d) garnet-cordierite-sillimanite migmatitic gneiss of Grand-Béréby GDB8; (e) garnet-staurolite-bearing micaschist of Kounoukou KOU7 and (f) potassic granite of San Pedro CIS62.

### 6.3. Archean crustal evolution in the Sassandra Cavally domain

The protolith of the Monogaga migmatitic gneiss sample MON4 dated at  $3328 \pm 13$  Ma shows a zircon  $\epsilon_{\text{Hf}}$  between +0.2 and +3.3. Migmatitic gneisses from the San Pedro and Monogaga samples exhibit protolith ages at  $3245 \pm 4$  Ma (SP11) and  $3238 \pm 4$  Ma (SP3B) and show a zircon  $\epsilon_{\text{Hf}}$  between +1.5 to -4.6 and +0.3 and -9.4 to -0.3 respectively (**Fig. 11**). These results point toward an early juvenile crust extraction at ca. 3300 Ma (MON4) immediately followed by reworking of older crustal components (SP11 and SP3B) the latter being highlighted by highly negative  $\epsilon_{\text{Hf}}$  values down to -9.4 (**Fig. 9a**).

Whereas slightly positive and negative  $\epsilon_{\text{Hf}}$  values may be related to the reworking of material emplaced at ca. 3300 Ma (MON4), the recorded  $\epsilon_{\text{Hf}}$  values for San Pedro sample (SP3B), extending to -9.4, are indicative of the reworking of an even older crustal precursor (**Fig. 9**). Depleted Mantle Hf model ages are severely limited by the multiple, unconstrained assumptions and uncertainties that tend to produce a bias towards artificially old model ages ([Vervoort and Kemp, 2016](#)). Accordingly, it is difficult to evaluate the age of the crustal precursor that contributed to the magmatic process.

One may assume the extraction of enriched material from the mantle early on, followed by the transformation of this dominantly basaltic protocrust into something progressively more felsic from ca. 3.8 Ga (e.g., [Patchett and Arndt, 1986](#); [Veizer and Jansen, 1979](#); [Vervoort et al., 2012](#)) (**Fig. 9**). Using a  $^{176}\text{Lu}/^{177}\text{Hf} = 0.0115$  age range for the precursor from which the zircons with negative  $\epsilon_{\text{Hf}}$  values may be loosely constrained as a Meso to Paleoproterozoic source (**Fig. 9**). Ages of the continental crust formation were obtained in the south-western part of the West African Craton (Kenema-Man domain) as early as ca. 3500 Ma ([Thiéblemont et al., 2001](#)). Further U-Pb evaporation zircon ages acquired in the Reguibat shield suggest a crustal growth period of the WAC prior to  $3515 \pm 15$  Ma ([Potrel et al., 1996](#)). While beyond the scope of this study, it is noteworthy that acquisition of Hf data from samples dated at ca. 3500 Ma would offer an opportunity to confirm or infirm the presence of such ancient juvenile crust extraction. More recently, the Lu-Hf data obtained by [Eglinger et al. \(2017\)](#) on Archean rocks from the northern

margin of the Leo-Man shield further documented the development of a juvenile crust from the Eoarchean.

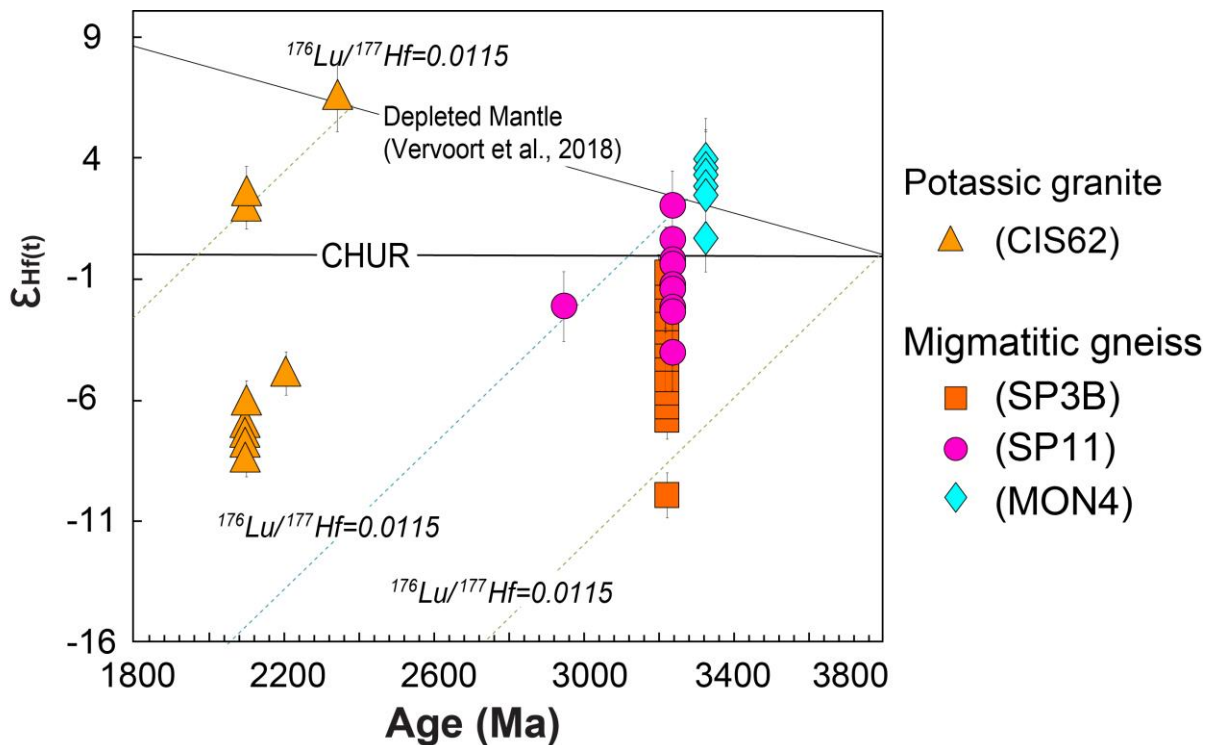


**Fig. 11.**  $\epsilon_{\text{Hf}(t)}$  vs.  $^{207}\text{Pb}/^{206}\text{Pb}$  age diagrams showing the ages of the protoliths of the San Pedro and Monogaga migmatitic gneisses and the San Pedro potassic granite.

#### 6.4. Proterozoic geochronological record of the Sassandra-Cavally domain

Four samples collected over the Sassandra-Cavally domain returned Paleoproterozoic ages (**Fig.10**). A sample of the potassic granite (CIS62) that appears emplaced both parallel to and cutting across the main synmigmatitic foliation of the San Pedro migmatitic gneiss returned concordant to near concordant analyses spreading in age from ca. 2312 Ma to ca. 2084 Ma with a crystallization age at  $2084 \pm 5$  Ma. This age is within uncertainty of the  $2076 \pm 6$  Ma metamorphic age from the Monogaga gneiss SP11. Such coeval relationship suggests that both the metamorphism and production of potassic melts likely developed during the partial melting recorded by the structure and mineral paragenesis of the host gneiss. Sample CIS62 has a potassic peraluminous granitic composition similar to the one intruding into the northern margin of the Archean Kenema-Man domain (Eglinger et al., 2017). Metamorphic reworking of Archean rocks during the Paleoproterozoic was also reported in the zone of Man (Caby et al., 2000; Kouamelan et al., 1997b; Pitra et al., 2010; Triboulet and Feybesse, 1998) with ages comparable to those found in this study.

Both the metamorphic age of the migmatitic gneiss and magmatic emplacement of potassic granite suites are also very close to the youngest ages of detrital zircons from the Kounoukou micaschist and Grand-Béréby paragneiss. The two metasedimentary samples both returned Paleoproterozoic age clusters. The sample of garnet-cordierite-sillimanite migmatitic gneiss of Grand-Béréby (GDB8) provides zircon ages ranging from ca. 2670 Ma to 2060 Ma. Whereas this sample presents Archean detrital zircons dated at ca. 2670 Ma ( $n = 1$ ) the remaining concordant zircons display an age spectrum ranging from ca. 2213 to 2060 Ma, which overlap the sequence of events encountered in the Baoule-Mossi domain. It is also noteworthy that the youngest grain dated in this sample yields an age of  $2069 \pm 4$  Ma. The other metasediment analysed in this study (garnet-staurolite-bearing micaschist of Kounoukou, KOU7), returned a comparable detrital zircon age spectrum ranging from ca. 2214 to 2082 Ma. Two hypotheses are possible to interpret the youngest ages: it could be either a maximum age for deposition of the sediment or the age of metamorphism of the sedimentary protolith. If these ages represent deposition ages, it suggests that the time lapse between sediment deposition and metamorphism during the Eburnean orogeny was very short. Alternatively, if these young ages are interpreted as metamorphic, the deposition age would then be ca. 2100 Ma, taking into account the main age peak at ca. 2109 Ma for KOU7. This hypothesis allows for a longer, and more realistic, time lapse between the deposition and metamorphism and is consistent with the time lag (ca. 20 Myrs) between the sediment deposition and their burial and metamorphism in the nearby Kedougou-Kenieba Inlier ([Kone et al., 2020](#)). Interestingly, no Archean detrital zircons with ages corresponding to the ages found in the migmatitic gneisses were identified there except for only one grain yielding  $2670 \pm 11$  Ma.

The results from our study further document the major crustal reworking process, including that of ancient Archean crustal domains that took place at the later stages of the Eburnean orogeny. Detrital zircons from both metasediments (garnet-cordierite-sillimanite migmatitic gneiss of Grand-Béréby, GDB8 and garnet-staurolite-bearing micaschist of Kounoukou, KOU7) returned  $\epsilon_{\text{Hf}}$  values between +0.0 and +5.5. Such  $\epsilon_{\text{Hf}}$  data highlights the broadly juvenile signature and echoes with results obtained in the Baoule-Mossi domain ([Parra-Avila et al., 2017](#)). In contrast, the ca. 2086 Ma old potassic granite (CIS62) intruding the San Pedro gneissic unit exhibits a population of inherited zircons with a hybrid Hf isotopic signature. In this rock,  $\epsilon_{\text{Hf}}$  form two distinct clusters between -4.9 and -8.5 ( $n = 6$ ) and between +1.9 and +6.5 ( $n = 3$ ) for zircons formed between ca. 2343 to 2100 Ma. Zircons with strongly negative  $\epsilon_{\text{Hf}}$  are darker in CL images than those with positive  $\epsilon_{\text{Hf}}$  which show lighter character in CL images. This hybrid isotopic signature is pointing towards both Paleoproterozoic juvenile input and reworking of

pre-existing, likely Archean, crust. The model ages for the Archean protolith(s) is broadly estimated between about 3.3 and 3.1 Ga (**Fig. 9**). This age bracket is consistent with the age distribution provided by the SASCA Archean gneisses. These results also echo with those obtained from the northern transect across the Kenema-Man domain margin. There, the inherited crustal reworking signature is further highlighted by the presence of inherited Archean zircons with U-Pb ages between ca. 2.87 and 3.09 Ga ([Eglinger et al., 2017](#)).

### **6.5. Regional implication**

The net influence of pre-existing Archean crust on the overall crustal evolutionary process in this Paleoproterozoic part of the West African Craton remains elusive, with most of the Baoulé-Mossi domain dominated by Proterozoic juvenile isotopic signature. Yet, the Lu-Hf isotopic data acquired in the Southern Mali and Western Burkina Faso by [Parra-Avila et al. \(2017\)](#) further indicate the local contribution of older crustal material potentially as old as ca. 2800 Ma. In the northern part of the Archean Kenema-Man domain, close to the limit of the Proterozoic Baoulé-Mossi domain of Guinea, the terranes appear to be largely reworked at ca. 2100 Ma ([Eglinger et al., 2017](#)). The presence of Archean xenocrysts in Paleoproterozoic granitic intrusions further suggests some degree of involvement of the Archean crust during the formation of Paleoproterozoic granitic magmas ([Abati et al., 2012](#); [Begg et al., 2009](#); [Block et al., 2016](#); [Petersson et al., 2016, 2018](#)). For example, Archean zircons between ca. 3.0 and 3.4 Ga were found in the Boboti pluton in the Kedougou-Kenieba Inlier ([Lambert-Smith et al., 2016](#)).

The Archean influence on crustal development in the West African Craton is also well documented in the southeast Baoulé Mossi domain. In Ghana, the Winneba pluton returned  $\epsilon_{\text{Hf}}$  and  $\epsilon_{\text{Nd}}$  values, indicative of an Archean crustal contribution ([Leube et al., 1990](#); [Taylor et al., 1992](#)). In-situ analyses conducted in Ghana highlighted  $\epsilon_{\text{Hf}}$  zircon signature attesting of a short-lived period of crustal reworking at ca. 2140 to 2130 Ma following an Eoeburnean (ca. 2250 Ma) juvenile accretion ([Block et al., 2016](#); [Petersson et al., 2016, 2018](#)).

The identification of Archean relics within the Sassandra-Cavally domain east of the Sassandra regional boundary and in southeastern Ghana ([Petersson et al., 2016](#)) highlights the prevalence of Archean blocks of various sizes and their influence on Paleoproterozoic crustal evolution. In the Sassandra-Cavally domain, the late magmatic reworking at ca. 2080 Ma is broadly coeval with that observed in the northern edge of the Kenema-Man domain, where granites analysed in the Suhum basin ([Petersson et al., 2016](#)) suggest significant reworking of Archean rocks starting from ca. 2113 Ma. Such time lag may attest to a diachronic assembly of several Archean

blocks with a westward migration of the magmatic front over the Eburnean orogeny (Parra-Avila et al., 2017) and further support a collisional tectonic model involving the docking between Archean and Paleoproterozoic blocks resulting in large-scale crustal thickening (Allibone et al., 2002, in press; Eglinger et al., 2017; Feybesse et al., 2006; Feybesse and Milési, 1994; Grenholm et al., 2019; Koffi, 2019; Wane et al., 2018).

The absence of Archean xenocrysts of the ages of the migmatitic gneisses of San Pedro and Monogaga (~3200-2800 Ma) in the Kounoukou misaschist and the Grand Béréby paragneiss is noteworthy as these lithologies are adjacent today. Such absence raises the question of the nature and timing of the contact between the Archean gneisses and Paleoproterozoic metasediments of the Sassandra-Cavally domain and suggests the sediments did not source the Archean basement. The two domains were assembled by collisional tectonics later during the Eburnean orogeny, which is documented by similar metamorphic ages in the migmatitic gneisses ( $2076 \pm 6$  Ma) and metasediments (from  $2082 \pm 4$  Ma to  $2069 \pm 4$  Ma) along with the magmatic age ( $2084 \pm 6$  Ma) of the potassic granite intruding the gneisses. Such relationship may be seen as key to further unravel tectonic process leading to the craton assembly.

## CONCLUSION

U-Pb and Lu-Hf isotope analyses on zircon from rocks of the SASCA domain located to the east of the Sassandra shear zone (Archean-Paleoproterozoic transition zone) allows to further constrain the timing of the continental crust extraction and illustrates the protracted crustal stabilization process that contributed to the emergence of continental landmasses in the Precambrian. The migmatitic gneisses of San Pedro and Monogaga contain essentially Archean zircons (U-Pb ages of ca. 3328 to 2812 Ma) with  $\epsilon_{\text{Hf}}$  values ranging from -12.6 to +3.8, pointing to early crustal growth and reworking of older, possibly Paleoarchean, crustal precursors. The spread of ages combined with  $^{176}\text{Hf}/^{177}\text{Hf}_t$  obtained on the Archean migmatitic gneiss point towards a 3.3 Ga age for the protolith followed by a 2.8 Ga led loss event (early migmatitization). Yet, a more complex scenario involving a prolonged period of dissolution/precipitation and/or crystallisation in the presence of melt over that period cannot be completely ruled out.

In Grand-Béréby and Kounoukou metasedimentary rocks were affected by high-temperature metamorphism reaching partial melting. U-Pb ages on zircons range from ca. 2213 to 2088 Ma with  $\epsilon_{\text{Hf}}$  values ranging from +0.0 to +5.5. These data suggest a second major period of crustal growth at this time. The granitic sample of the San Pedro area, dated at  $2084 \pm 6$  Ma, exhibits a hybrid isotopic signature with  $\epsilon_{\text{Hf}}$  values forming two distinct clusters between -4.9 and -8.5

and between +2.2 and +6.5 for inherited zircon grains dated between ca. 2343 to 2100 Ma. This is indicative of a mixed signature involving reworking of Archean domains and juvenile Paleoproterozoic input. The San Pedro granite intrusion is coeval with peak metamorphic conditions and the migmatitisation of the Monogaga Archean gneiss, which is dated at  $2076 \pm 6$  Ma. This age is within error of the youngest Proterozoic ages identified in KOU7 ( $2082 \pm 4$  Ma) and GDB8 ( $2069 \pm 4$  Ma). These young ages may accordingly reflect metamorphism rather than maximum deposition age. By comparison, in the Baoulé-Mossi domain the plutonic activity occurred between ca. 2250 and ca. 2060 Ma (Agyei et al., 2009; Delor et al., 1995; Feybesse et al., 2006; Lahondère et al., 2002; Schwartz and Melcher, 2003; Tshibubudze et al., 2013; Liégeois et al., 1991; Parra-Avila et al., 2018, 2017; Thébaud et al., 2019; Tshibubudze et al., 2013; Eglinger et al., 2017; Mériaud et al., 2020). The ages of emplacement of felsic intrusions in the Baoulé-Mossi domain are associated with two orogenic cycles namely the Eoeburnean orogeny (ca. 2250–2150 Ma) and the Eburnean orogeny (ca. 2135–2100 Ma) (Liégeois et al., 1991; Parra-Avila et al., 2018, 2017; Thébaud et al., 2019; Tshibubudze et al., 2013). It has been proposed that the docking of the Leo-Man shield onto the Baoulé-Mossi domain occurred from ca. 2095 Ma and may coincide with a period of lithospheric delamination leading to the widespread emplacement of potassic two-mica granites (Eglinger et al., 2017) as well as extrusive bi-modal volcanism (Mériaud et al., 2020). The second period of crustal growth recorded in the SASCA domain is highlighting the influence of this thermal event.

Our conclusions further highlight the local contribution of Archean crustal domains in the foundation of the West African Craton in the Paleoproterozoic (Begg et al., 2009; Parra-Avila et al., 2019, 2016; Petersson et al., 2018). The proportion of the Archean reworked crustal component, documented by both U-Pb zircon ages and Hf model ages, seems to be more important than was registered by the Sm/Nd isotopic system, which suggested exclusively a Paleoproterozoic juvenile character of these rocks (Boher et al., 1992). The West African Craton consists in the assembly of Paleoarchean and Neoproterozoic crustal domains that were partially reworked in the Paleoproterozoic during the Eburnean orogeny.

## ACKNOWLEDGEMENTS

This project is part of a PhD study of A.Y.K. funded by the T2GEM project (Geophysical and Geochemical Technologies for Mineral Exploration). We wish to gratefully acknowledge AMIRA International and the industry sponsors, for their support of the WAXI project (P934B). We are also appreciative of the contribution of the various geological surveys department of mines in West Africa as sponsors in kind of WAXI. The authors acknowledge the French

National Research Institute for Sustainable Development (IRD, LMI MINERWA Laboratory for Responsible Mining in West Africa) for funding a part of this research project. The authors wish to thank Brad McDonald (Curtin University) for technical assistance during analysis. GeoHistory Facility instruments were funded via an Australian Geophysical Observing System grant provided to AuScope Pty Ltd. by the AQ44 Australian Education Investment Fund program. The NPII multi-collector and laser ablation system at UWA were obtained via funding from the Australian Research Council LIEF program (LE150100013). NT would like to acknowledge the Hammond and Nisbet trust for its support. The authors gratefully acknowledge two anonymous reviewers and Bernard Bingen for their constructive reviews. We also thank Chris Fisher and Oscar Laurent for their insights into the isotopic geochemistry which greatly helped improve the quality of this manuscript.

## REFERENCES

- Abati, J., Aghzer, A.M., Gerdes, A., Ennih, N., 2012. Insights on the crustal evolution of the West African Craton from Hf isotopes in detrital zircons from the Anti-Atlas belt. *Precambrian Res.* 212, 263–274.
- Abouchami, W., Boher, M., Michard, A., Albarede, F., 1990. A major 2.1 Ga event of mafic magmatism in west Africa: An Early stage of crustal accretion. *J. Geophys. Res.* 95, 17605. <https://doi.org/10.1029/JB095iB11p17605>
- Agyei, D.J., Loh, G.K., Boamah, K.O., Baba, M., Hirdes, W., Toloczyki, M., Davis, D.W., 2009. Geological map of Ghana 1: 1,000,000. *Geol. Surv. Dep. Ghana.*
- Allibone, A., Lawrence, D., Scott, J., Fanning, M., Lambert-Smith, J., Stenhouse, P., Harbidge, R., Vargas, C., Rose Turnbull, R., Holliday, J., in press. Early Paleoproterozoic gold deposits of the Loulo district, western Mali. *SEG Spec. Publ.*
- Allibone, A., Teasdale, J., Cameron, G., Etheridge, M., Uttley, P., Soboh, A., Appiah-Kubi, J., Adanu, A., Arthur, R., Mamphey, J., Odoom, B., Zuta, J., Tsikata, A., Pataye, F., Famiyeh, S., Lamb, E., 2002. Timing and structural controls on gold mineralization at the Bogoso Gold Mine, Ghana, West Africa. *Econ. Geol.* 97, 949–969. <https://doi.org/10.2113/gsecongeo.97.5.949>
- Ama Salah, I., Liegeois, J.-P., Pouclet, A., 1996. Evolution d'un arc insulaire océanique birimien précoce au Liptako nigérien (Sirba): géologie, géochronologie et géochimie. *J. Afr. Earth Sci.* 22, 235–254. [https://doi.org/10.1016/0899-5362\(96\)00016-4](https://doi.org/10.1016/0899-5362(96)00016-4)
- Amelin, Y., Lee, D.-C., Halliday, A.N., 2000. Early-middle archaean crustal evolution deduced from Lu-Hf and U-Pb isotopic studies of single zircon grains. *Geochim. Cosmochim. Acta* 64, 4205–4225. [https://doi.org/10.1016/S0016-7037\(00\)00493-2](https://doi.org/10.1016/S0016-7037(00)00493-2)
- Amelin, Y., Lee, D.-C., Halliday, A.N., Pidgeon, R.T., 1999. Nature of the Earth's earliest crust from hafnium isotopes in single detrital zircons. *Nature* 399, 252–255.

- Armstrong, R.A., Compston, W., Retief, E.A., Williams, I.S., Welke, H.J., 1991. Zircon ion microprobe studies bearing on the age and evolution of the Witwatersrand triad. *Precambrian Res.* 53, 243–266. [https://doi.org/10.1016/0301-9268\(91\)90074-K](https://doi.org/10.1016/0301-9268(91)90074-K)
- Auvray, B., Peucat, J.-J., Potrel, A., Burg, J.-P., Caruba, C., Dars, R., Lo, K., 1992. Données géochronologiques nouvelles sur l'Archéen de l'Amsaga (Dorsale Réguibat, Mauritanie). *Données Géochronologiques Nouv. Sur Archéen Amsaga Dorsale Réguibat Maurit.* 315, 63–70.
- Baratoux, L., Metelka, V., Naba, S., Jessell, M.W., Grégoire, M., Ganne, J., 2011. Juvenile Paleoproterozoic crust evolution during the Eburnean orogeny (~2.2–2.0Ga), western Burkina Faso. *Precambrian Res.* 191, 18–45. <https://doi.org/10.1016/j.precamres.2011.08.010>
- Barth, M.G., Rudnick, R.L., Carlson, R.W., Horn, I., McDonough, W.F., 2002. Re • Os and U • Pb geochronological constraints on the eclogite–tonalite connection in the Archean Man Shield, West Africa. *Precambrian Res.* 118, 267–283. [https://doi.org/10.1016/S0301-9268\(02\)00111-0](https://doi.org/10.1016/S0301-9268(02)00111-0)
- Beckinsale, R., Gale, N., Pankhurst, R., Macfarlane, A., Crow, M., Arthurs, J., Wilkinson, A., 1980. Discordant Rb • Sr and Pb • Pb whole rock isochron ages for the Archaean basement of Sierra Leone. *Precambrian Res.* 13, 63–76. [https://doi.org/10.1016/0301-9268\(80\)90059-5](https://doi.org/10.1016/0301-9268(80)90059-5)
- Begg, G.C., Griffin, W.L., Natapov, L.M., O'Reilly, S.Y., Grand, S.P., O'Neill, C.J., Hronsky, J.M.A., Djomani, Y.P., Swain, C.J., Deen, T., 2009. The lithospheric architecture of Africa: Seismic tomography, mantle petrology, and tectonic evolution. *Geosphere* 5, 23–50.
- Belousova, E.A., Kostitsyn, Y.A., Griffin, W.L., Begg, G.C., O'Reilly, S.Y., Pearson, N.J., 2010. The growth of the continental crust: Constraints from zircon Hf-isotope data. *Lithos* 119, 457–466. <https://doi.org/10.1016/j.lithos.2010.07.024>
- Berger, J., Diot, H., Lo, K., Ohnenstetter, D., Féménias, O., Pivin, M., Demaiffe, D., Bernard, A., Charlier, B., 2013. Petrogenesis of Archean PGM-bearing chromitites and associated ultramafic–mafic–anorthositic rocks from the Guelb el Azib layered complex (West African craton, Mauritania). *Precambrian Res.* 224, 612–628. <https://doi.org/10.1016/j.precamres.2012.10.005>
- Bering, D., Brinckmann, J., Camara, N.D., Diawara, M., Gast, L., Keita, S., 1998. Etude évaluation de l'inventaire des ressources minérales de Guinée. Bundesanst. Geowiss. Rohst. Dir. Natl. Rech. Géologique Hydrocarb. Hanovre Conakry.
- Bessoles, B., 1977. Géologie de l'Afrique. Le craton Ouest Africain, Mémoire du BRGM.
- Béziat, D., Bourges, F., Debat, P., Lompo, M., Martin, F., Tollon, F., 2000. A Paleoproterozoic ultramafic-mafic assemblage and associated volcanic rocks of the Boromo greenstone belt: fractionates originating from island-arc volcanic activity in the West African craton. *Precambrian Res.* 101, 25–47.
- Block, S., Baratoux, L., Zeh, A., Laurent, O., Bruguier, O., Jessell, M., Ailleres, L., Sagna, R., Parra-Avila, L.A., Bosch, D., 2016. Paleoproterozoic juvenile crust formation and stabilisation in the south-eastern West African Craton (Ghana); New insights from U-Pb-Hf zircon data and geochemistry. *Precambrian Res.* 287, 1–30. <https://doi.org/10.1016/j.precamres.2016.10.011>

- Block, S., Ganne, J., Baratoux, L., Zeh, A., Parra-Avila, L.A., Jessell, M., Ailleres, L., Siebenaller, L., 2015. Petrological and geochronological constraints on lower crust exhumation during Paleoproterozoic (Eburnean) orogeny, NW Ghana, West African Craton. *J. Metamorph. Geol.* 33, 463–494. <https://doi.org/10.1111/jmg.12129>
- Boher, M., Abouchami, W., Michard, A., Albarede, F., Arndt, N.T., 1992. Crustal growth in West Africa at 2.1 Ga. *J. Geophys. Res. Solid Earth* 97, 345–369. <https://doi.org/10.1029/91JB01640>
- Bouilhol, P., Jagoutz, O., Hanchar, J.M., Dudas, F.O., 2013. Dating the India–Eurasia collision through arc magmatic records. *Earth Planet. Sci. Lett.* 366, 163–175.
- Bouilhol, P., Schaltegger, U., Chiaradia, M., Ovtcharova, M., Stracke, A., Burg, J.-P., Dawood, H., 2011. Timing of juvenile arc crust formation and evolution in the Sapat Complex (Kohistan–Pakistan). *Chem. Geol.* 280, 243–256.
- Bucher, K., Grapes, R., 2011. Metamorphism of Pelitic Rocks (Metapelites), in: Bucher, K., Grapes, R. (Eds.), *Petrogenesis of Metamorphic Rocks*. Springer, Berlin, Heidelberg, pp. 257–313. [https://doi.org/10.1007/978-3-540-74169-5\\_7](https://doi.org/10.1007/978-3-540-74169-5_7)
- Caby, R., Delor, C., Agoh, O., 2000. Lithology, structure and metamorphism of the Birimian formations in the Odienné area (Ivory Coast): the major role played by plutonic diapirism and strike-slip faulting at the border of the Man Craton. *J. Afr. Earth Sci.* 30, 351–374.
- Cahen, L., Snelling, N.J., Delhal, J., Vail, J.R., Bonhomme, M., Ledent, D., 1984. *The geochronology and evolution of Africa (PhD Thesis)*. Clarendon, Oxford.
- Camil, J., 1984. *Péetrographie, chronologie des ensembles granulitiques archéens et formations associées de la région de Man (Côte d’Ivoire) Implication pour l’histoire géologique du Craton Ouest-Africain*. PhD thesis, Abidjan, 306 p.
- Camil, J., 1981. Un exemple de métamorphisme prograde de la base du faciès des amphibolites au faciès des granulites dans la région de Man (Ouest de la Côte d’Ivoire). *C. R. l’Académie Sci. Paris* 93, 513–518.
- Camil, J., Tempier, P., Pin, C., 1983. Age Libérien des quartzites a magnétite de la région de Man (Côte d’Ivoire) et leur place dans l’orogène Libérien. *C. R. l’Académie Sci. Paris* 296, 149–151.
- Condie, K.C., 2013. *Plate tectonics & crustal evolution*. Elsevier.
- Condie, K.C., Aster, R.C., 2013. Refinement of the supercontinent cycle with Hf, Nd and Sr isotopes. *Geosci. Front.* 4, 667–680.
- Condie, K.C., Bickford, M.E., Aster, R.C., Belousova, E., Scholl, D.W., 2011. Episodic zircon ages, Hf isotopic composition, and the preservation rate of continental crust. *Bulletin* 123, 951–957.
- da Rosa-Costa, L.T., Lafon, J.M., Delor, C., 2006. Zircon geochronology and Sm–Nd isotopic study: Further constraints for the Archean and Paleoproterozoic geodynamical evolution of the southeastern Guiana Shield, north of Amazonian Craton, Brazil. *Gondwana Res.* 10, 277–300. <https://doi.org/10.1016/j.gr.2006.02.012>

- De Waele, B., Lacorde, M., Vergara, F., Chan, G., 2015. New insights on proterozoic tectonics and sedimentation along the peri-Gondwanan West African margin based on zircon U–Pb SHRIMP geochronology. *Precambrian Res., Supercontinental Cycles and Geodynamics* 259, 156–175. <https://doi.org/10.1016/j.precamres.2014.08.008>
- Delor, C., Lahondère, D., Egal, E., Lafon, J.-M., Cocherie, A., Guerrot, C., Rossi, P., Truffert, C., Théveniaut, H., Phillips, D., de AVELAR, V.G., 2003. Transamazonian crustal growth and reworking as revealed 53.
- Delor, C., Siméon, Y., Vidal, M., 1995. Peri-plutonic gravity driven deformations and transcurrent tectonics between 2.2 and 2.1 By: a case study from the Birimian Cycle in Ivory Coast, in: EUG. p. 102.
- Doumbia, S., Pouclet, A., Kouamelan, A., Peucat, J.J., Vidal, M., Delor, C., 1998. Petrogenesis of juvenile-type Birimian (Paleoproterozoic) granitoids in Central Côte-d'Ivoire, West Africa: geochemistry and geochronology. *Precambrian Res.* 87, 33–63. [https://doi.org/10.1016/S0301-9268\(97\)00201-5](https://doi.org/10.1016/S0301-9268(97)00201-5)
- Egal, E., Thiéblemont, D., Lahondère, D., Guerrot, C., Costea, C.A., Iliescu, D., Delor, C., Goujou, J.-C., Lafon, J.M., Tegye, M., Diaby, S., Kolié, P., 2002. Late Eburnean granitization and tectonics along the western and northwestern margin of the Archean Kénéma–Man domain (Guinea, West African Craton). *Precambrian Res.* 117, 57–84. [https://doi.org/10.1016/S0301-9268\(02\)00060-8](https://doi.org/10.1016/S0301-9268(02)00060-8)
- Eglinger, A., Thébaud, N., Zeh, A., Davis, J., Miller, J., Parra-Avila, L.A., Loucks, R., McCuaig, C., Belousova, E., 2017. New insights into the crustal growth of the Paleoproterozoic margin of the Archean Kéména–Man domain, West African craton (Guinea): Implications for gold mineral system. *Precambrian Res.* 292, 258–289. <https://doi.org/10.1016/j.precamres.2016.11.012>
- Feybesse, J.-L., Billa, M., Guerrot, C., Duguey, E., Lescuyer, J.-L., Milesi, J.-P., Bouchot, V., 2006. The paleoproterozoic Ghanaian province: Geodynamic model and ore controls, including regional stress modeling. *Precambrian Res.* 149, 149–196. <https://doi.org/10.1016/j.precamres.2006.06.003>
- Feybesse, J.-L., Milési, J.-P., 1994. The Archaean/Proterozoic contact zone in West Africa: a mountain belt of décollement thrusting and folding on a continental margin related to 2.1 Ga convergence of Archaean cratons? *Precambrian Res.* 69, 199–227. [https://doi.org/10.1016/0301-9268\(94\)90087-6](https://doi.org/10.1016/0301-9268(94)90087-6)
- Fisher, C.M., Vervoort, J.D., DuFrane, S.A., 2014. Accurate Hf isotope determinations of complex zircons using the “laser ablation split stream” method. *Geochem. Geophys. Geosystems* 15, 121–139.
- Ganne, J., Gerbault, M., Block, S., 2014. Thermo-mechanical modeling of lower crust exhumation—Constraints from the metamorphic record of the Palaeoproterozoic Eburnean orogeny, West African Craton. *Precambrian Res.* 243, 88–109. <https://doi.org/10.1016/j.precamres.2013.12.016>
- Gärtner, A., Youbi, N., Villeneuve, M., Sagawe, A., Hofmann, M., Mahmoudi, A., Boumehdi, M.A., Linnemann, U., 2017. The zircon evidence of temporally changing sediment transport—

the NW Gondwana margin during Cambrian to Devonian time (Aoucert and Smara areas, Moroccan Sahara). *Int. J. Earth Sci.* 106, 2747–2769. <https://doi.org/10.1007/s00531-017-1457-x>

Gasquet, D., Barbey, P., Adou, M., Paquette, J.-L., 2003. Structure, Sr–Nd isotope geochemistry and zircon U–Pb geochronology of the granitoids of the Dabakala area (Côte d’Ivoire): evidence for a 2.3 Ga crustal growth event in the Palaeoproterozoic of West Africa? *Precambrian Res.* 127, 329–354.

Gouedji, F., Picard, C., Coulibaly, Y., Audet, M.-A., Auge, T., Goncalves, P., Paquette, J.-L., Ouattara, N., 2014. The Samapleu mafic-ultramafic intrusion and its Ni-Cu-PGE mineralization: an Eburnean (2.09 Ga) feeder dyke to the Yacouba layered complex (Man Archean craton, western Ivory Coast). *Bull. Société Géologique Fr.* 185, 393–411. <https://doi.org/10.2113/gssgfbull.185.6.393>

Grenholm, M., 2014. The Birimian event in the Baoulé Mossi domain (West African Craton): regional and global context. *Diss. Geol. Lund Univ.*

Grenholm, M., Jessell, M., Thébaud, N., 2019. A geodynamic model for the Paleoproterozoic (ca. 2.27–1.96 Ga) Birimian Orogen of the southern West African Craton – Insights into an evolving accretionary-collisional orogenic system. *Earth-Sci. Rev.* 192, 138–193. <https://doi.org/10.1016/j.earscirev.2019.02.006>

Griffin, W.L., Wang, X., Jackson, S.E., Pearson, N.J., O’Reilly, S.Y., Xu, X., Zhou, X., 2002. Zircon chemistry and magma mixing, SE China: in-situ analysis of Hf isotopes, Tonglu and Pingtan igneous complexes. *Lithos* 61, 237–269.

Gruau, G., Martin, H., Leveque, B., Capdevila, R., Marot, A., 1985. Rb—Sr and Sm—Nd geochronology of lower Proterozoic granite—greenstone terrains in French Guiana, South America. *Precambrian Res.* 30, 63–80. [https://doi.org/10.1016/0301-9268\(85\)90029-4](https://doi.org/10.1016/0301-9268(85)90029-4)

Guergouz, C., Martin, L., Vanderhaeghe, O., Thébaud, N., Fiorentini, M., 2018. Zircon and monazite petrochronologic record of prolonged amphibolite to granulite facies metamorphism in the Ivrea-Verbano and Strona-Ceneri Zones, NW Italy. *Lithos* 308, 1–18.

Harrison, T.M., Blichert-Toft, J., Müller, W., Albarede, F., Holden, P., Mojzsis, S.J., 2005. Heterogeneous Hadean hafnium: evidence of continental crust at 4.4 to 4.5 Ga. *Science* 310, 1947–1950.

Harrison, T.M., Schmitt, A.K., McCulloch, M.T., Lovera, O.M., 2008. Early ( $\geq 4.5$  Ga) formation of terrestrial crust: Lu–Hf,  $\delta^{18}\text{O}$ , and Ti thermometry results for Hadean zircons. *Earth Planet. Sci. Lett.* 268, 476–486.

Hawkesworth, C.J., Dhuime, B., Pietranik, A.B., Cawood, P.A., Kemp, A.I.S., Storey, C.D., 2010. The generation and evolution of the continental crust. *J. Geol. Soc.* 167, 229–248. <https://doi.org/10.1144/0016-76492009-072>

Hawkesworth, C.J., Kemp, A.I.S., 2006. Evolution of the continental crust. *Nature* 443, 811–817.

- Hirdes, W., Davis, D.W., Eisenlohr, B.N., 1992. Reassessment of Proterozoic granitoid ages in Ghana on the basis of U/Pb zircon and monazite dating. *Precambrian Res.* 56, 89–96. [https://doi.org/10.1016/0301-9268\(92\)90085-3](https://doi.org/10.1016/0301-9268(92)90085-3)
- Hirdes, W., Davis, D.W., Lüdtke, G., Konan, G., 1996. Two generations of Birimian (Paleoproterozoic) volcanic belts in northeastern Côte d’Ivoire (West Africa): consequences for the ‘Birimian controversy.’ *Precambrian Res.* 80, 173–191. [https://doi.org/10.1016/S0301-9268\(96\)00011-3](https://doi.org/10.1016/S0301-9268(96)00011-3)
- Jessell, M., Santoul, J., Baratoux, L., Youbi, N., Ernst, R.E., Metelka, V., Miller, J., Perrouty, S., 2015. An updated map of West African mafic dykes. *J. Afr. Earth Sci., Tectonics, mineralisation and regolith evolution of the West African Craton* 112, 440–450. <https://doi.org/10.1016/j.jafrearsci.2015.01.007>
- Jessell, M.W., Begg, G.C., Miller, M.S., 2016. The geophysical signatures of the West African Craton. *Precambrian Res., Craton to Regional-scale analysis of the Birimian of West Africa* 274, 3–24. <https://doi.org/10.1016/j.precamres.2015.08.010>
- John, T., Klemd, R., Hirdes, W., Loh, G., 1999. The metamorphic evolution of the paleoproterozoic (Birimian) volcanic Ashanti belt (Ghana, West Africa). *Precambrian Res.* 98, 11–30.
- Kemp, A.I.S., Wilde, S.A., Hawkesworth, C.J., Coath, C.D., Nemchin, A., Pidgeon, R.T., Vervoort, J.D., DuFrane, S.A., 2010. Hadean crustal evolution revisited: new constraints from Pb–Hf isotope systematics of the Jack Hills zircons. *Earth Planet. Sci. Lett.* 296, 45–56.
- Koffi, A.Y., 2019. Evolution tectono-métamorphique du Craton Ouest Africain : Exemple du secteur de Grand-Béréby a Sassandra (Sud-Ouest de la Côte d’Ivoire). *Mém. Univ. Félix Houphouët-Boigny UFR STRM* 351p.
- Koffi, G.R.-S., Kouamelan, A.N., Allialy, M.E., Coulibaly, Y., Peucat, J.-J., 2020. Re-evaluation of Leonian and Liberian events in the geodynamical evolution of the Man-Leo Shield (West African Craton). *Precambrian Res.* 338, 105582. <https://doi.org/10.1016/j.precamres.2019.105582>
- Kone, J., Vanderhaeghe, O., Diatta, F., Baratoux, L., Thebaud, N., Bruguier, O., Ndiaye, P.M., Duchene, S., Pitra, P., Ganne, J., 2020. Source and deposition age of the Dialé-Daléma metasedimentary series (Kédougou-Kéniéba Inlier, Senegal) constrained by U–Pb geochronology on detrital zircon grains. *J. Afr. Earth Sci.* 165, 103801. <https://doi.org/10.1016/j.jafrearsci.2020.103801>
- Kouamelan, A.-N., 1996. Géochronologie et Géochimie des Formations Archéennes et Protérozoïques de la Dorsale de Man en Côte d’Ivoire. Implications pour la Transition Archéen-Protérozoïque (phdthesis). Université Rennes 1.
- Kouamelan, A.N., Djro, S.C., Allialy, M.E., Paquette, J.-L., Peucat, J.-J., 2015. The oldest rock of Ivory Coast. *J. Afr. Earth Sci.* 103, 65–70. <https://doi.org/10.1016/j.jafrearsci.2014.12.004>
- Kouamelan, A.N., Kra, K.S.A., Djro, S.C., Paquette, J.-L., Peucat, J.-J., 2018. The Logoualé Band: A large Archean crustal block in the Kenema-Man domain (Man-Leo rise, West African Craton) remobilized during Eburnean orogeny (2.05 Ga). *J. Afr. Earth Sci., Paleoproterozoic*

Kouamelan, Delor, C., Peucat, J.-J., 1997a. Geochronological evidence for reworking of Archean terrains during the Early Proterozoic (2.1 Ga) in the western Côte d'Ivoire (Man Rise-West African Craton). *Precambrian Res.* 86, 177–199. [https://doi.org/10.1016/S0301-9268\(97\)00043-0](https://doi.org/10.1016/S0301-9268(97)00043-0)

Kouamelan, Peucat, J.-J., Delor, C., 1997b. Reliques archéennes (3,15 Ga) au sein du magmatisme birimien (2,1 Ga) de Côte d'Ivoire, craton ouest-africain. *Reliques Archéennes 315 Ga Au Sein Magmat. Birimien 21 Ga Côte Ivoire Craton Ouest-Afr.* 324, 719–727.

Křibek, B., Šýkorová, I., Machovič, V., Laufek, F., 2008. Graphitization of organic matter and fluid-deposited graphite in Palaeoproterozoic (Birimian) black shales of the Kaya-Goren greenstone belt (Burkina Faso, West Africa). *J. Metamorph. Geol.* 26, 937–958.

Lahondère, D., Thiéblemont, D., Goujou, J.C., Roger, J., Moussine-Pouchkine, A., Le Metour, J., Cocherie, A., Guerrot, C., 2003. Notice explicative des cartes géologiques et gîtologiques à 1/200 000 et 1/500 000 du Nord de la Mauritanie. DMG Ministère Mines Ind. Nouakchott 1.

Lahondère, D., Thiéblemont, D., Tegye, M., Guerrot, C., Diabate, B., 2002. First evidence of early Birimian (2.21 Ga) volcanic activity in Upper Guinea: the volcanics and associated rocks of the Niani suite. *J. Afr. Earth Sci.* 35, 417–431.

Lambert-Smith, J.S., Lawrence, D.M., Müller, W., Treloar, P.J., 2016. Palaeotectonic setting of the south-eastern Kédougou-Kéniéba Inlier, West Africa: New insights from igneous trace element geochemistry and U-Pb zircon ages. *Precambrian Res.* 274, 110–135.

Laurent, O., Martin, H., Moyen, J.F., Doucelance, R., 2014. The diversity and evolution of late-Archean granitoids: Evidence for the onset of “modern-style” plate tectonics between 3.0 and 2.5Ga. *Lithos* 205, 208–235. <https://doi.org/10.1016/j.lithos.2014.06.012>

Laurent, O., ZEH, A., Delmelle, N., Vander Auwera, J., Wilson, A., D'abzac, F.-X., 2016. The role of Archean tectonics in shaping Paleoproterozoic intraplate magmatism and ore deposits in the Kaapvaal craton (southern Africa): a case study from the 2.05 Ga Schiel complex. *GB2016* 90.

Ledru, P., Johan, V., Milési, J.P., Tegye, M., 1994. Markers of the last stages of the Palaeoproterozoic collision: evidence for a 2 Ga continent involving circum-South Atlantic provinces. *Precambrian Res.* 69, 169–191.

Leube, A., Hirdes, W., Mauer, R., Kesse, G.O., 1990. The early Proterozoic Birimian Supergroup of Ghana and some aspects of its associated gold mineralization. *Precambrian Res.* 46, 139–165.

Liégeois, J.-P., Claessens, W., Camara, D., Klerkx, J., 1991. Short-lived Eburnian orogeny in southern Mali. *Geology, tectonics, U-Pb and Rb-Sr geochronology.* *Precambrian Res.* 50, 111–136.

Maas, R., Kinny, P.D., Williams, I.S., Froude, D.O., Compston, W., 1992. The Earth's oldest known crust: a geochronological and geochemical study of 3900–4200 Ma old detrital zircons

- from Mt. Narryer and Jack Hills, Western Australia. *Geochim. Cosmochim. Acta* 56, 1281–1300.
- MacFarlane, A., MJ, C., AF, W., 1981. The geology and mineral resource of Northern Sierra Leone.
- Masurel, Q., Thébaud, N., Miller, J., Ulrich, S., 2017. The tectono-magmatic framework to gold mineralisation in the Sadiola-Yatela gold camp and implications for the paleotectonic setting of the Kédougou-Kénieba inlier, West Africa. *Precambrian Res.* 292, 35–56.
- McDonough, W.F., Sun, S.-S., Ringwood, A.E., Jagoutz, E., Hofmann, A.W., 1992. Potassium, rubidium, and cesium in the Earth and Moon and the evolution of the mantle of the Earth. *Geochim. Cosmochim. Acta* 56, 1001–1012.
- McKenzie, D., Priestley, K., 2008. The influence of lithospheric thickness variations on continental evolution. *Lithos* 102, 1–11.
- Meert, J.G., 2012. What's in a name? The Columbia (Paleopangaea/Nuna) supercontinent. *Gondwana Res., Advances in High-Resolution Ion-Microprobe Geochronology* 21, 987–993. <https://doi.org/10.1016/j.gr.2011.12.002>
- Mériaud, N., Thébaud, N., Masurel, Q., Hayman, P., Jessell, M., Kemp, A., Evans, N.J., Fisher, C.M., Scott, P.M., 2020. Lithostratigraphic evolution of the Bandamian Volcanic Cycle in central Côte d'Ivoire: Insights into the late Eburnean magmatic resurgence and its geodynamic implications. *Precambrian Res.* 347, 105847.
- Milési, J.-P., Henry, C., Sylvain, J.-P., 1989. Minéralisations aurifères de l'Afrique de l'ouest leurs relations avec l'évolution lithostructurale au Proterozoïque inférieur. Bureau de recherches géologiques et minières.
- Milési, J.-P., Ledru, P., Feybesse, J.-L., Dommange, A., Marcoux, E., 1992. Early Proterozoic ore deposits and tectonics of the Birimian orogenic belt, West Africa. *Precambrian Res.* 58, 305–344.
- Milhomem Neto, J.M., Lafon, J.-M., 2020. Crustal growth and reworking of Archean crust within the Rhyacian domains of the southeastern Guiana Shield, Brazil: Evidence from zircon U–Pb–Hf and whole-rock Sm–Nd geochronology. *J. South Am. Earth Sci.* 103, 102740. <https://doi.org/10.1016/j.jsames.2020.102740>
- Milhomem Neto, J.M., Lafon, J.-M., 2019. Zircon U-Pb and Lu-Hf isotope constraints on Archean crustal evolution in Southeastern Guyana Shield. *Geosci. Front.* 10, 1477–1506. <https://doi.org/10.1016/j.gsf.2018.09.012>
- Moyen, J.-F., Martin, H., 2012. Forty years of TTG research. *Lithos* 148, 312–336.
- Nance, R.D., Murphy, J.B., Santosh, M., 2014. The supercontinent cycle: A retrospective essay. *Gondwana Res.* 25, 4–29. <https://doi.org/10.1016/j.gr.2012.12.026>
- Nebel-Jacobsen, Y., Münker, C., Nebel, O., Gerdes, A., Mezger, K., Nelson, D.R., 2010. Reworking of Earth's first crust: constraints from Hf isotopes in Archean zircons from Mt. Narryer, Australia. *Precambrian Res.* 182, 175–186.

- O'Connor, J.T., 1965. A classification for quartz-rich igneous rocks based on feldspar ratio. *US Geol. Surv. Prof Pap.* 525-B 79-84.
- Papon, A., 1973. Géologie et minéralisations du Sud-Ouest de la Côte d'Ivoire : Synthèse des travaux de l'opération SASCA.
- Parra-Avila, L.A., Baratoux, L., Eglinger, A., Fiorentini, M.L., Block, S., 2019. The Eburnean magmatic evolution across the Baoulé-Mossi domain: geodynamic implications for the West African Craton. *Precambrian Res.* 332, 105392.
- Parra-Avila, L.A., Belousova, E., Fiorentini, M.L., Baratoux, L., Davis, J., Miller, J., McCuaig, T.C., 2016. Crustal evolution of the Paleoproterozoic Birimian terranes of the Baoulé-Mossi domain, southern West African Craton: U–Pb and Hf-isotope studies of detrital zircons. *Precambrian Res., Craton to Regional-scale analysis of the Birimian of West Africa* 274, 25–60. <https://doi.org/10.1016/j.precamres.2015.09.005>
- Parra-Avila, L.A., Belousova, E., Fiorentini, M.L., Eglinger, A., Block, S., Miller, J., 2018. Zircon Hf and O-isotope constraints on the evolution of the Paleoproterozoic Baoulé-Mossi domain of the southern West African Craton. *Precambrian Res.* 306, 174–188.
- Parra-Avila, L.A., Kemp, A.I., Fiorentini, M.L., Belousova, E., Baratoux, L., Block, S., Jessell, M., Bruguier, O., Begg, G.C., Miller, J., 2017. The geochronological evolution of the Paleoproterozoic Baoulé-Mossi domain of the southern West African Craton. *Precambrian Res.* 300, 1–27.
- Patchett, P.J., Arndt, N.T., 1986. Nd isotopes and tectonics of 1.9-1.7 Ga crustal genesis. *Earth Planet. Sci. Lett.* 78, 329–338.
- Petersson, A., Scherstén, A., Gerdes, A., 2018. Extensive reworking of Archaean crust within the Birimian terrane in Ghana as revealed by combined zircon U–Pb and Lu–Hf isotopes. *Geosci. Front., Lid Tectonics* 9, 173–189. <https://doi.org/10.1016/j.gsf.2017.02.006>
- Petersson, A., Scherstén, A., Kemp, A.I.S., Kristinsdóttir, B., Kalvig, P., Anum, S., 2016. Zircon U–Pb–Hf evidence for subduction related crustal growth and reworking of Archaean crust within the Palaeoproterozoic Birimian terrane, West African Craton, SE Ghana. *Precambrian Res.* 275, 286–309. <https://doi.org/10.1016/j.precamres.2016.01.006>
- Peucat, J.-J., Capdevila, R., Drareni, A., Mahdjoub, Y., Kahoui, M., 2005. The Eglab massif in the West African Craton (Algeria), an original segment of the Eburnean orogenic belt: petrology, geochemistry and geochronology. *Precambrian Res.* 136, 309–352. <https://doi.org/10.1016/j.precamres.2004.12.002>
- Pitra, P., Kouamelan, A.N., Balleve, M., Peucat, J.-J., 2010. Palaeoproterozoic high-pressure granulite overprint of the Archean continental crust: evidence for homogeneous crustal thickening (Man Rise, Ivory Coast). *J. Metamorph. Geol.* 28, 41–58.
- Pons, J., Barbey, P., Dupuis, D., Léger, J.M., 1995. Mechanisms of pluton emplacement and structural evolution of a 2.1 Ga juvenile continental crust: the Birimian of southwestern Niger. *Precambrian Res.* 70, 281–301.
- Potrel, A., Peucat, J.J., Fanning, C.M., 1998. Archean crustal evolution of the West African Craton: example of the Amsaga Area (Reguibat Rise). U • Pb and Sm • Nd evidence for crustal

growth and recycling. *Precambrian Res.* 90, 107–117. [https://doi.org/10.1016/S0301-9268\(98\)00044-8](https://doi.org/10.1016/S0301-9268(98)00044-8)

Potrel, A., Peucat, J.J., Fanning, C.M., Auvray, B., Burg, J.P., Caruba, C., 1996. 3.5 Ga old terranes in the West African craton, Mauritania. *J. Geol. Soc.* 153, 507–510.

Poucllet, A., Doumbia, S., Vidal, M., 2006. Geodynamic setting of the Birimian volcanism in central Ivory Coast (western Africa) and its place in the Palaeoproterozoic evolution of the Man Shield. *Bull. Société Géologique Fr.* 177, 105–121. <https://doi.org/10.2113/gssgfbull.177.2.105>

Pystin, A., Pystina, J., 2015. The early Precambrian history of rock metamorphism in the Urals segment of crust. *Int. Geol. Rev.* 57, 1650–1659.

Roberts, N.M., Spencer, C.J., 2015. The zircon archive of continent formation through time. *Geol. Soc. Lond. Spec. Publ.* 389, 197–225.

Rocci, G., 1965. Essai d'interprétation de mesures géochronologiques. La structure de l'Ouest Africain. *Sci. Terre* 10, 461–478.

Rollinson, H., 2018. The geochemical evolution of Archaean felsic gneisses in the West African Craton in Sierra Leone. *J. Afr. Earth Sci.* 143, 28–39. <https://doi.org/10.1016/j.jafrearsci.2018.03.018>

Rollinson, H., 2016. Archaean crustal evolution in West Africa: A new synthesis of the Archaean geology in Sierra Leone, Liberia, Guinea and Ivory Coast. *Precambrian Res.* 281, 1–12. <https://doi.org/10.1016/j.precamres.2016.05.005>

Rollinson, H.R., Cliff, R.A., 1982. New Rb-Sr age determinations on the Archaean basement of Eastern Sierra Leone. *Precambrian Res.* 17, 63–72. [https://doi.org/10.1016/0301-9268\(82\)90154-1](https://doi.org/10.1016/0301-9268(82)90154-1)

Rubatto, D., 2002. Zircon trace element geochemistry: partitioning with garnet and the link between U–Pb ages and metamorphism. *Chem. Geol.* 184, 123–138.

Santosh, M., 2010. Assembling North China Craton within the Columbia supercontinent: The role of double-sided subduction. *Precambrian Res.* 178, 149–167. <https://doi.org/10.1016/j.precamres.2010.02.003>

Schwartz, M.O., Melcher, F., 2003. The Perkoa zinc deposit, Burkina Faso. *Econ. Geol.* 98, 1463–1485.

Skublov, S.G., Lobach-Zhuchenko, S.B., Guseva, N.S., Gembitskaya, I.M., Tolmachyova, E.V., 2009. Distribution of rare-earth and rare elements in zircons from the miaskite lamproites of the Panozero intrusion in Central Karelia. *Geochemistry* 958–971.

Soumaila, A., Garba, Z., 2006. Le métamorphisme des formations de la ceinture de roches vertes birimienne (paleoproterozoïque) de Diagorou-Darbani (Liptako, Niger, Afrique de l'Ouest). *Afr. Geosci. Rev.* 13, 107.

Sun, S.-S., McDonough, W.F., 1989. Chemical and isotopic systematics of oceanic basalts: implications for mantle composition and processes. *Geol. Soc. Lond. Spec. Publ.* 42, 313–345.

Tagini, B., 1971. Esquisse structurale de la Côte d'Ivoire. Essai de géotectonique régionale. *These Univ Lausanne Soc. Etat Pour Dev. Min. Cote Ivoire.*

- Tapsoba, B., Lo, C.-H., Jahn, B.-M., Chung, S.-L., Wenmenga, U., Iizuka, Y., 2013. Chemical and Sr–Nd isotopic compositions and zircon U–Pb ages of the Birimian granitoids from NE Burkina Faso, West African Craton: Implications on the geodynamic setting and crustal evolution. *Precambrian Res.* 224, 364–396.
- Taylor, P.N., Moorbath, S., Leube, A., Hirdes, W., 1992. Early Proterozoic crustal evolution in the birimian of Ghana: constraints from geochronology and isotope geochemistry. *Precambrian Res.* 56, 97–111. [https://doi.org/10.1016/0301-9268\(92\)90086-4](https://doi.org/10.1016/0301-9268(92)90086-4)
- Thébaud, N., Allibone, A., Masurel, Q., Eglinger, A., Davis, J., André-Mayer, A.S., Miller, J., Jessell, M., 2019. The Paleoproterozoic (Rhyacian) gold deposits of West Africa.
- Thiéblemont, D., 2016. An updated geological map of Africa at 1/10 000 000 scale. Presented at the 35th International Geological Congress : IGC 2016.
- Thiéblemont, D., Delor, C., Cocherie, A., Lafon, J.M., Goujou, J.C., Baldé, A., Bah, M., Sané, H., Mark Fanning, C., 2001. A 3.5 Ga granite–gneiss basement in Guinea: further evidence for early archean accretion within the West African Craton. *Precambrian Res.* 108, 179–194. [https://doi.org/10.1016/S0301-9268\(00\)00160-1](https://doi.org/10.1016/S0301-9268(00)00160-1)
- Thiéblemont, D., Goujou, J.C., Egal, E., Cocherie, A., Delor, C., Lafon, J.M., Fanning, C.M., 2004. Archean evolution of the Leo Rise and its Eburnean reworking. *J. Afr. Earth Sci., Key Points on African Geology* 39, 97–104. <https://doi.org/10.1016/j.jafrearsci.2004.07.059>
- Triboulet, C., Feybesse, J.-L., 1998. Les métabasites birimiennes et archéennes de la région de Toulepleu-Itty (Côte-d’Ivoire): des roches portées à 8 kbar ( $\approx$  24 km) et 14 kbar ( $\approx$  42 km) au Paléoprotérozoïque. *Comptes Rendus Académie Sci.-Ser. IIA-Earth Planet. Sci.* 327, 61–66.
- Tshibubudze, A., Hein, K.A.A., McCuaig, T.C., 2015. The relative and absolute chronology of strato-tectonic events in the Gorom-Gorom granitoid terrane and Oudalan-Gorouol belt, northeast Burkina Faso. *J. Afr. Earth Sci., Tectonics, mineralisation and regolith evolution of the West African Craton* 112, 382–418. <https://doi.org/10.1016/j.jafrearsci.2015.04.008>
- Tshibubudze, A., Hein, K.A.A., Peters, L.F.H., Woolfe, A.J., McCuaig, T.C., 2013. Oldest U–Pb crystallisation age for the West African Craton From the Oudalan-Gorouol Belt of Burkina Faso. *South Afr. J. Geol.* 116, 169–181.
- Vachette, M., G, R., J, S., JPH, C., J, M., B, S., C, T., 1973. Ages radiométriques Rb/Sr, de 2000 à 1700 Ma, de séries métamorphiques et granites intrusifs Précambriens dans la partie n et ne de la dorsale Réguibat (Mauritanie septentrionale).
- Vanderhaeghe, O., Guergouz, C., Fabre, C., Duchêne, S., Baratoux, D., 2019. Secular cooling and crystallization of partially molten Archean continental crust over 1 Ga. *Comptes Rendus Geosci., New aspects of magma storage and transfer* 351, 562–573. <https://doi.org/10.1016/j.crte.2019.07.002>
- Vanderhaeghe, O., Ledru, P., Thiéblemont, D., Egal, E., Cocherie, A., Tegye, M., Milési, J.-P., 1998. Contrasting mechanism of crustal growth: Geodynamic evolution of the Paleoproterozoic granite–greenstone belts of French Guiana. *Precambrian Res.* 92, 165–193. [https://doi.org/10.1016/S0301-9268\(98\)00074-6](https://doi.org/10.1016/S0301-9268(98)00074-6)

Veizer, J., Jansen, S.L., 1979. Basement and sedimentary recycling and continental evolution. *J. Geol.* 87, 341–370.

Vervoort, J.D., Kemp, A.I., 2016. Clarifying the zircon Hf isotope record of crust–mantle evolution. *Chem. Geol.* 425, 65–75.

Vervoort, J.D., Kemp, A.I., Fisher, C.M., 2018. Hf isotope constraints on evolution of the depleted mantle and growth of continental crust 2018, V23A-07.

Vervoort, J.D., Kemp, T., Fisher, C.M., 2012. No significant production of continental crust prior to 3.8 Ga, in: *AGU Fall Meeting Abstracts*. pp. T11B-2570.

Vidal, M., Gumiaux, C., Cagnard, F., Pouclet, A., Ouattara, G., Pichon, M., 2009. Evolution of a Paleoproterozoic “weak type” orogeny in the West African Craton (Ivory Coast). *Tectonophysics, Hot orogens* 477, 145–159. <https://doi.org/10.1016/j.tecto.2009.02.010>

Wane, O., Liégeois, J.-P., Thébaud, N., Miller, J., Metelka, V., Jessell, M., 2018. The onset of the Eburnean collision with the Kenema-Man craton evidenced by plutonic and volcanosedimentary rock record of the Massigui region, southern Mali. *Precambrian Res.* 305, 444–478. <https://doi.org/10.1016/j.precamres.2017.11.008>

WAXI report, AMIRA Global, 2018. West African Exploration Initiative Stage 3, AMIRA International Limited Level 2 271 William St Melbourne VIC 3000 Australia, p.925.

Woodhead, J., Hergt, J., Shelley, M., Eggins, S., Kemp, R., 2004. Zircon Hf-isotope analysis with an excimer laser, depth profiling, ablation of complex geometries, and concomitant age estimation. *Chem. Geol.* 209, 121–135.

Zeh, A., Stern, R.A., Gerdes, A., 2014. The oldest zircons of Africa—Their U–Pb–Hf–O isotope and trace element systematics, and implications for Hadean to Archean crust–mantle evolution. *Precambrian Res.* 241, 203–230.

Zhao, G., Cawood, P.A., Wilde, S.A., Sun, M., 2002. Review of global 2.1–1.8 Ga orogens: implications for a pre-Rodinia supercontinent. *Earth-Sci. Rev.* 59, 125–162. [https://doi.org/10.1016/S0012-8252\(02\)00073-9](https://doi.org/10.1016/S0012-8252(02)00073-9)